Simulating Electron Transfer on Noisy Quantum Computers: A Scalable Approach to Open Quantum Systems

Marvin Gajewski,[1, 2] Alejandro D. Somoza,[1, 2] Gary Schmiedinghoff,[3]
Pascal Stadler,[4] Michael Marthaler,[4] and Birger Horstmann[1, 2, 5, *]

[1]*Institute of Engineering Thermodynamics, German Aerospace Center (DLR), Wilhelm-Runge-Str. 10, 89081 Ulm, Germany*
[2]*Helmholtz Institute Ulm, Helmholtzstr. 11, 89081 Ulm, Germany*
[3]*Institute of Software Technology, German Aerospace Center (DLR), Linder Höhe, 51147 Köln, Germany*
[4]*HQS Quantum Simulations GmbH, Rintheimer Straße 23, 76131 Karlsruhe, Germany*
[5]*Department of Physics, Ulm University, Albert-Einstein-Allee 11, 89081 Ulm, Germany*

Simulating large electronic networks with vibrational environments remains a fundamental challenge due to the long lifetimes of electronic-vibrational (vibronic) excitations on the picosecond scale. Quantum computers are a promising platform to simulate the dynamics of open quantum systems aided by intrinsic hardware-noise, with successful demonstrations of models with two electronic sites. We simulated a microscopic model of electron-transfer (ET) with a single donor and up to nine acceptor sites on a superconducting processor of IBM, using a model-specific error mitigation scheme. Our results using up to 20 qubits reveal a probability of ET that is well aligned with classical calculations where electronic and vibronic transfer resonances can be identified at the expected driving forces. We conducted 10 independent experiments per system size on different days, accounting for hourly fluctuations in error rates. We find that the most important ingredient for large-scale simulations is a large number of available qubits connected by high-fidelity gates, with coherence times above the threshold set by the target open system. Because the vibronic mechanism of electron transfer is entanglement-driven, our simulation is a natural application-based benchmark, in which the hardware capacity to produce and sustain entanglement is quantified by the maximum system size for which the hardware produces accurate results.

I. INTRODUCTION

The transformation of the energy and transportation industries demands the development of novel and powerful simulation tools such as quantum computers, supporting the design of new materials operating across a wide range of environmental conditions. Kinetic theories at thermal equilibrium fail to accurately capture transfer rates in relevant scenarios, such as the inverted region in the Marcus theory of electron transfer [1–5]. This regime is for example relevant for batteries with large overpotentials, indicative of high reorganization energies and complex solvation shells [6–11] that are linked to dissipative processes. A proper understanding of heat loss at the microscopic scale is crucial in the engineering of next-generation devices for energy storage and production.

Nonequilibrium processes on the picosecond scale (10^{-12} s) are coming into focus thanks to the increasing time resolution of spectroscopic techniques [12, 13]. Nonequilibrium quantum effects are a promising route to increase the efficiency of energy materials thanks to their unusual thermodynamic properties [14], such as long-lived electronic-vibrational (vibronic) coherence [15, 16] or the slow cooling of hot-carriers [17–20]. These processes are found to strongly affect the efficiency and directionality of electron transfer (ET) between reactant molecules and electrode surfaces [21–30], as well as the ultrafast charge separation in organic photovoltaics [31]

and photosynthetic systems [32]. Polaron formation in battery electrodes [33–40] and perovskites is also thought to strongly influence the transport of charges [36, 41–47].

Quantum computers bring the potential to simulate the nonequilibrium dynamics of materials in operando conditions to reveal new insights into the underlying mechanisms that govern their performance [48]. As such models are described by open quantum systems, noise processes in the quantum hardware that are compatible with the target open quantum system can be exploited [49–51], while unwanted sources of noise are mitigated insofar as possible [52, 53]. There is a growing interest in using dissipation and structured noise as a resource in quantum computing, from the acceleration of variational optimization workflows [54] to the engineering of initial states [55–59]. In particular, novel quantum platforms that naturally realize quantized oscillators via bosonic elements in the hardware have the potential to become powerful toolboxes for the simulation of open quantum systems [60–63], avoiding resource-intensive boson-to-qubit encodings [51]. On trapped ions, vibronic electron transfer with tunable dissipation has been demonstrated for dimer systems [64, 65], as well as the engineering of structured environments for spin-boson models [66, 67]. Although quantum algorithms for the simulation of extended networks like the Holstein model on trapped ions have been put forth [68, 69], experimental demonstrations with large problem sizes are still notoriously challenging.

We focus on the non-equilibrium dynamics of vibronic networks and show simulations with up to ten electronic sites. Ultrafast ET ($\lesssim$ 100 fs) can be observed in the
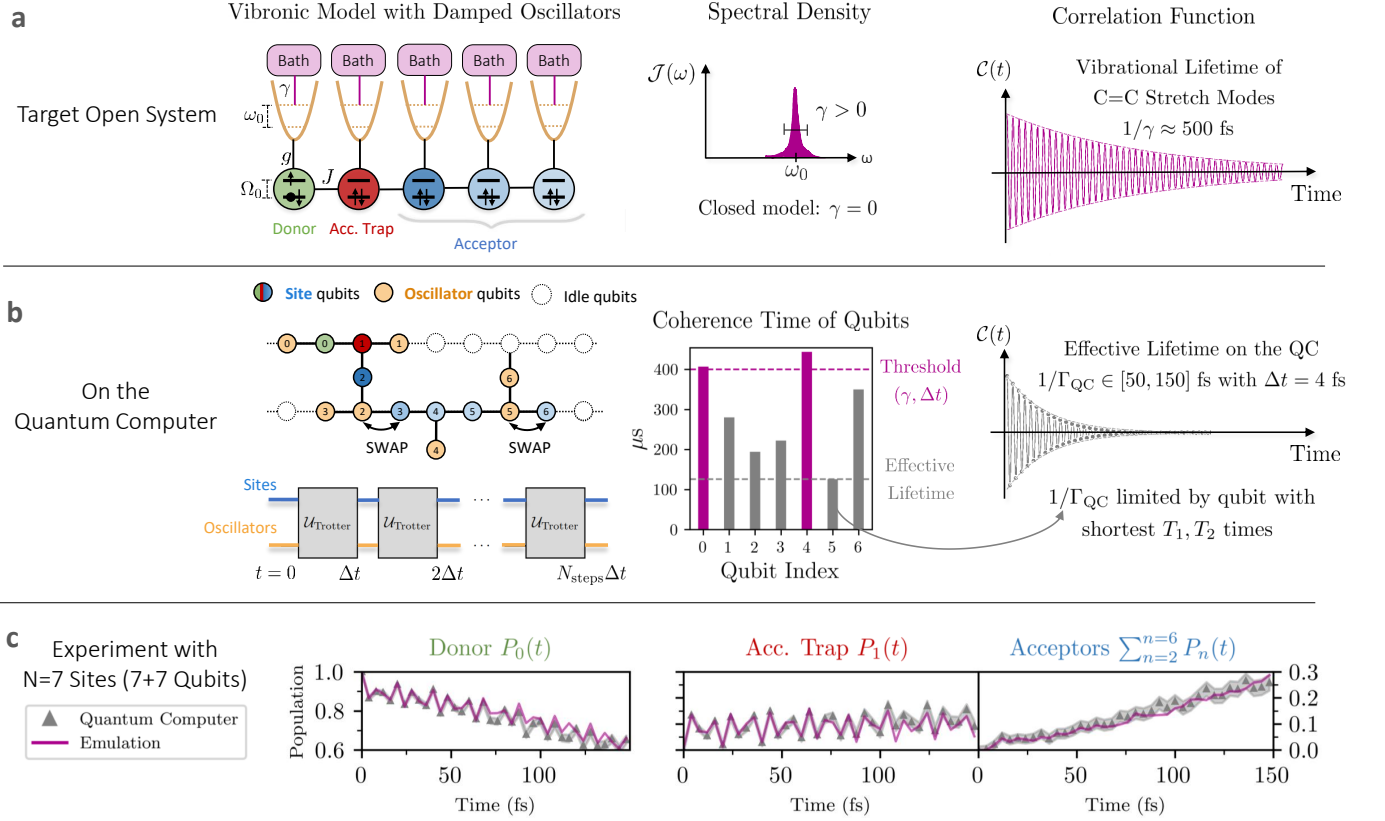
* birger.horstmann@dlr.de

FIG. 1. **Algorithm overview. a.** The left panel shows a schematic of the one-dimensional LVC Hamiltonian with nearest-neighbors electronic interactions of coupling strength J, where each site of energy Ω_n is locally coupled to a single quantum harmonic oscillator of frequency ω_0 with vibronic coupling strength g. These oscillators may be damped by independent vibrational environments with a rate γ that are characterised by the same spectral density $\mathcal{J}(\omega)$ (Eq. (5)), shown in the center panel. For closed vibronic systems the damping rate is strictly zero ($\gamma = 0$). The width of the peak around ω_0 determines the lifetime $1/\gamma$ of vibrational excitations and the duration of system-environment correlations (non-Markovian dynamics), which can be observed in the right panel with the bath correlation function $\mathcal{C}(t)$ (Eq. (8)). **b.** On the quantum computer, each electronic site is mapped to a single qubit while oscillators are mapped to qubits using a boson-to-spin encoding (left panel). Trotterized circuits corresponding to the closed model ($\gamma = 0$) simulate the dynamics of the open model ($\gamma > 0$) with a time step Δt due to the intrinsic damping of oscillator qubits. The center panel illustrates a distribution of coherence times of qubits involved in the circuit, together with the threshold required to simulate weakly damped C=C stretch modes. Note that the threshold depends on the choice of Δt and the circuit execution time on the hardware (Eq. (13)). We found that the shortest T_1 or T_2 time determines the effective damping rate Γ_{QC}, that lies for the simulations presented here between $(50\,\mathrm{fs})^{-1}$ and $(150\,\mathrm{fs})^{-1}$ (right panel). **c.** Experimental results for vibronic electron transfer (see Sec. III B) are shown for 7 sites (14 qubits) in comparison to an emulation of the open model with damping of the oscillator qubits corresponding to a rate of $\gamma = (150\,\mathrm{fs})^{-1}$.

non-Markovian dynamics, whose duration is determined by the finite lifetime of vibrational motion [70]. While ultrafast ET can happen via purely electronic resonance between donor and acceptor states [71], it can remarkably also occur via vibronic resonance mediated by the coherent interaction of electrons and vibrations like C=C stretch modes in organic photovoltaics [72], whose frequencies are one order of magnitude above room temperature. Such effects are supported by pump-probe experiments showing clear evidence of long-lived ($\lesssim 0.5$ ps) vibronic coherence in the charge separation of electronic excitations [31, 73–78].

Our approach uses the pseudomode formalism to simulate the dynamics of the open vibronic system [79–

83], as depicted in Fig. 1 **a.**, by incorporating a single damped oscillator (pseudomode) at each electronic site. As each oscillator is locally coupled to its own Markovian bath, one is able to engineer arbitrary models of non-Markovian dynamics in the reduced system of interest, the electronic network. One can substantially lower the memory requirements in numerical simulations when combining pseudomodes with tensor networks techniques [12, 84, 85], because local damping naturally destroys correlations between oscillators. This logic can be extended to quantum algorithms that exploit local dissipation as a quantum resource. By using damped oscillators in the simulation of open quantum systems on NISQ computers, entanglement requirements may be lowered and adapted

to the lifetime of system-environment correlations [86].

When simulating the Trotterized dynamics of the closed model on the quantum computer with a time step Δt as shown in Fig. 1 **b**, the intrinsic noise of the quantum processor will imprint an effective damping rate Γ_{QC}, which is connected to the T_1, T_2 times of the involved qubits (see Eq. (13)). While this approach is possible for a small number of qubits, the intrinsic variations of T_1, T_2 times among superconducting qubits limits the amount of available qubits above this threshold. As depicted in the histogram of Fig. 1 **b**, qubits with the shortest T_1, T_2 times will strongly influence the effective rate Γ_{QC} in the quantum computer. Note that target models with stronger damping rates ($\gamma \gg \Gamma_{QC}$) can be implemented either via delay instructions on environment qubits [59] or alternatively, by coupling the latter to an ancillary qubit with periodic reset operations [87]. However, simulations of target models with longer vibrational lifetimes ($\gamma \ll \Gamma_{QC}$) cannot be reproduced without countermeasures or improving gate fidelities. Also, for a faithful simulation only qubits that are used to encode oscillators should be subject to dissipation, so noise on other qubits will require mitigation.

In this work, we simulate a microscopic model of electron transfer on the superconducting quantum computer IBM_AACHEN, where an electronic chain of two-level systems corresponding to donor and acceptor sites is coupled to local vibrations. Our experimental results reproduce ET dynamics on up to 10 electronic sites (20 qubits) and lead to an effective lifetime $1/\Gamma_{QC}$ that lies between 50 and 150 fs (Fig. 1 **b**), approaching the long-lived motion of intramolecular vibrational modes in organic molecules ($1/\gamma \gtrsim 500$ fs), a fundamental challenge in classical simulations of open quantum systems where low damping rates render perturbative methods highly inaccurate.

In Sec. II we introduce the model and describe the method of Trotterized open quantum dynamics on the quantum computer. Experimental results from a IBM Heron-type quantum processor are presented in Sec. III, where Sec. III A shows simulation of different ET mechanisms for 5 sites and Sec. III B discusses the scaling behaviour for up to 10 sites (20 qubits).

II. METHODS

In this section, we first present the linear vibronic coupling (LVC) Hamiltonian used to simulate the donor-acceptor interface with local coupling to oscillators with high frequencies $\omega_0 = 1500\,\mathrm{cm}^{-1} \approx 186$ meV. Then we introduce damped harmonic oscillators (pseudomodes) as a tool for simulating non-perturbative dynamics and finally, we describe the noisy quantum algorithm that reproduces this dynamics on the quantum computer.
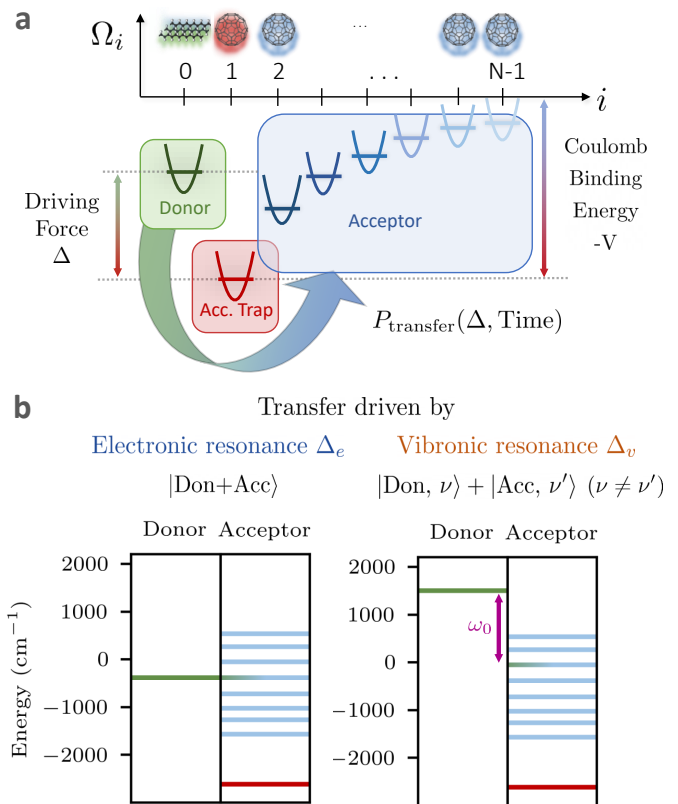

FIG. 2. **Microscopic model of the donor-acceptor chain and mechanisms of electronic and vibronic ET.** **a.** Schematic of the one-dimensional donor-acceptor interface with vibronic coupling to high-frequency, intramolecular C=C stretch modes. We vary the driving force Δ of the donor site ($n = 0$) to study the probability of electron transfer $P_{\mathrm{transfer}}(\Delta, \mathrm{Time})$ to the acceptor sites ($n > 1$). **b.** Donor energy and eigenenergies of the acceptor subsystem $\hat{H}_{\mathrm{el}}^{(\mathrm{Acc.})}$ (see Eq. (7)) for typical electronic and vibronic resonances. Both mechanisms induce ultrafast ET by creating superpositions of states with mixed donor/acceptor character. For the vibronic case (right-hand side), the superposition is created by coherent electron-oscillator (vibronic) coupling.

A. Target Open Quantum System

We consider a microscopic model of electron transfer from a single donor to $N - 1$ acceptor sites, coupled with nearest-neighbor electronic interactions (see Fig. 1 **a**). The excitation initially sits at the donor site ($n = 0$), and the first acceptor site ($n = 1$) acts as an energetic trap that competes with succesful charge separation. In the thermodynamic limit ($N \to \infty$), this constitutes the archetypal problem in the theory of electron transfer where a single donor is coupled to a continuous band of acceptor states [88].

The Hamiltonian parameters are chosen to model the ultrafast charge separation in a prototypical donor-acceptor blend from organic photovoltaics, consisting of a donor polymer like P3HT (Poly(3-hexylthiophene)) and

functionalized fullerenes like PCBM ([6,6]-phenyl-C61-butyric acid methyl ester) as acceptor molecules [72]. As represented by colored circles in Fig. 1 **a**, each molecule is treated as a two-level system that corresponds to its highest occupied (HOMO) and lowest unnoccupied (LUMO) molecular orbitals. The coupling between LUMO levels leads to electronic hopping between neighboring sites.

The initial state is given by a single electron-hole pair at the donor site (shown in green in Fig. 2 **a**), after which the electron may transfer to the acceptor molecules, while the hole is assumed to be frozen at the donor because of its lower mobility. This allows us to focus on the dynamics of the electron in the Coulomb potential that is induced by the hole, reflecting the bound nature of electron-hole pairs (excitons) in organic molecules. Charge separation is thought to take place faster than the creation of excitons via the absorption of photons in the donor. It is therefore common to assume that the dynamics remain in the single-excitation manifold at all times. The Hamiltonian incorporates both electronic and vibrational degrees of freedom, and is given by

$$\hat{H} = \hat{H}_{\text{el}} + \hat{H}_{\text{vib}} + \hat{H}_{\text{el-vib}}. \tag{1}$$

The electronic part of the Hamiltonian is modeled as a tight-binding chain $\hat{H}_{\text{el}}$

$$\hat{H}_{\text{el}} = \sum_{n=0}^{N-1} \Omega_n \, \hat{a}_n^\dagger \hat{a}_n + \sum_{n=0}^{N-2} J \left(\hat{a}_n^\dagger \hat{a}_{n+1} + \hat{a}_{n+1}^\dagger \hat{a}_n \right), \tag{2}$$

where $J = 500$ cm^{-1} is the coupling strength between sites, Ω_0 is the energy of the LUMO level of the single donor site, $\Omega_n = -V/n$ ($n \geq 1$) is the LUMO energy of the n-th acceptor site, $V = 2420$ cm^{-1} is the Coulomb binding energy ($V = |\Omega_1 - \Omega_n|$ for $n \to \infty$) and $\hat{a}_n^\dagger$ ($\hat{a}_n$) are the creation (annihilation) operators for an electron on site n. The local energy levels Ω_n are visualized in Fig. 2 **a**, where the first acceptor site ($n = 1$) clearly constitutes an energetic trap.

In general, the vibrational part of the Hamiltonian $\hat{H}_{\text{vib}}$ couples each electronic site n locally to a set of M_n quantum harmonic oscillators

$$\hat{H}_{\text{vib}} = \sum_{n=0}^{N-1} \sum_{m=0}^{M_n-1} \omega_{n,m} \, \hat{b}_{n,m}^\dagger \hat{b}_{n,m}, \tag{3}$$

where $\hat{b}_{n,m}^\dagger$ and $\hat{b}_{n,m}$ are the creation and annihilation operators for the m-th vibrational oscillator at site n, and frequency $\omega_{n,m}$. The vibronic coupling term $\hat{H}_{\text{el-vib}}$ describes the interaction between the electronic states and oscillators

$$\hat{H}_{\text{el-vib}} = \sum_{n=0}^{N-1} \sum_{m=0}^{M_n-1} g_{n,m} \left(\hat{a}_n^\dagger \hat{a}_n \otimes (\hat{b}_{n,m}^\dagger + \hat{b}_{n,m}) \right), \tag{4}$$

where $g_{n,m}$ is the vibronic coupling strength between the n-th site and the m-th vibrational oscillator.

The interaction between site n and its local vibrational environment is captured in the spectral density function

$$\mathcal{J}_n(\omega) = \sum_{m=0}^{M_n-1} g_{n,m}^2 \delta(\omega - \omega_{n,m}), \tag{5}$$

that becomes a continuous function in the thermodynamic limit $M_n \to \infty$ of the bath. We focus on modeling high-frequency, intramolecular vibrations like C=C stretch modes that are intrinsic to organic molecules. Therefore, we assume that every site is coupled to identical vibrational environments that are independent from each other

$$\mathcal{J}_n(\omega) \equiv \mathcal{J}(\omega) \text{ for all } n \in [0, N-1], \tag{6}$$

and are characterized by a single Lorentzian peak around $\omega_{n,0} \equiv \omega_0 = 1500$ cm^{-1} and vibronic coupling strength $g_{n,0} \equiv g = \omega_0 \sqrt{s}$, where $s = 0.05$ is the dimensionless Huang-Rhys factor. The choice of a single oscillator per site ($M = 1$, $\hat{b}_n \equiv \hat{b}_{n,0}$) we use to model this single-peak $\mathcal{J}(\omega)$ will be motivated in the following section along the theory of pseudomodes. However, note that the quantum algorithm presented in Sec. II C also works with a generic vibronic Hamiltonian. Further note that despite the assumption of a single-excitation, the occupied Hilbert space of the vibronic Hamiltonian in Eq. (1) generally scales exponentially with the system size N because of vibronic terms.

We probe two different mechanisms for ET (electronic vs. vibronic), depending on the driving force $\Delta = \Omega_0 - \Omega_1$ (see Eq. (2)), as depicted in Fig. 2 **b**. For ultrafast ET via purely electronic resonances, vibronic coupling is not required. The electronic resonances occur at driving forces Δ_e (see left panel of Fig. 2 **b**), where the donor energy Ω_0 is resonant with an eigenstate of the acceptor subsystem

$$\hat{H}_{\text{el}}^{(\text{Acc.})} = \sum_{n=1}^{N-1} \Omega_n \, \hat{a}_n^\dagger \hat{a}_n + \sum_{n=1}^{N-2} J \left(\hat{a}_n^\dagger \hat{a}_{n+1} + \hat{a}_{n+1}^\dagger \hat{a}_n \right), \tag{7}$$

defined in the same manner as $\hat{H}_{\text{el}}$, but restricted in the sums to $n > 0$ to exclude the donor site at $n = 0$. Ultrafast ET based on vibronic resonances requires vibronic coupling ($g > 0$) and occurs for driving forces $\Delta_v \approx \Delta_e + \omega_0$, when the energy difference between the donor and one of the acceptor eigenstates of $\hat{H}_{\text{el}}^{(\text{Acc.})}$ is matched by the energy ω_0 of a vibrational excitation. The mechanism of vibronic ET is thus driven by a non-separable (entangled) superposition of electronic and vibrational excitations, as depicted in the right panel of Fig. 2 **b**) and explained in further detail in App. A.

B. Pseudomode Description of the Vibrational Environment

The lifetime of vibrational excitations is inversely proportional to the width of the peak in the spectral density

$\mathcal{J}(\omega)$ (see Fig. 1 **b**). This width also determines the duration of system-environment correlations as illustrated by the decay of the correlation function of the environment [89]

$$\mathcal{C}(t) = \int_0^\infty d\omega \, \mathcal{J}(\omega) \left(\coth \frac{\beta\omega}{2} \cos \omega t - \mathrm{i} \sin \omega t \right), \quad (8)$$

where β is the inverse temperature (see Fig. 1 **a**). We fix the temperature to zero, where the bath correlation function $\mathcal{C}(t)$ and the spectral density $\mathcal{J}(\omega)$ form a Fourier pair. Incorporating finite temperatures in simulations would require the introduction of a low-frequency background that complicates the pseudomode treatment. As shown in [72], thermal effects only become apparent after 150 fs, suppressing electronic resonances at high driving forces which require longer evolution to be resolved. In contrast, vibronic resonances are very robust against thermal effects, because they are driven by long-lived, intramolecular vibrations whose frequencies ($\omega_0 = 1500 \, \mathrm{cm}^{-1}$) are much higher than room temperature ($k_B T_{\mathrm{room}} \approx 200 \, \mathrm{cm}^{-1}$).

A broadened peak in the spectral density $\mathcal{J}(\omega)$, corresponding to a finite lifetime of vibrational excitations, can be captured in unitary dynamics using an infinite amount of oscillators ($M \to \infty$) around the frequency ω_0 of the associated peak. An equivalent and simpler approach to reproduce such a broadened peak is achieved by coupling a single oscillator ($M = 1$, $b_n \equiv b_{n,1}$) with frequency ω_0 to a secondary bath (see Fig. 1 **b**). Such a damped oscillator is called a *pseudomode* [79–83].

The resulting dynamics are governed by the following master equation for the density matrix

$$\frac{d\hat{\rho}}{dt} = -\frac{\mathrm{i}}{\hbar}[\hat{H}, \hat{\rho}] + \mathcal{L}(\hat{\rho}), \quad (9)$$

where $\hat{H}$ is the Hamiltonian of the total vibronic system in Eq. (1) and $\mathcal{L}(\hat{\rho})$ represents the Lindblad superoperator

$$\mathcal{L}(\hat{\rho}) = \sum_{n=0}^{N-1} \gamma_n \left(\hat{b}_n \, \hat{\rho} \, \hat{b}_n^\dagger - \frac{1}{2} \{ \hat{b}_n^\dagger \, \hat{b}_n, \hat{\rho} \} \right), \quad (10)$$

that describes the damping of the n-th oscillator due to its coupling to an auxiliary bath with a rate γ_n (see Fig. 1 **b**). As thermal effects are negligible, only amplitude damping towards the ground state is considered in Eq. (10).

After tracing out the vibrational degrees of freedom, this approach allows to engineer non-Markovian dynamics in the reduced state of the electronic system ($\hat{\rho}_{\mathrm{el}} = \mathrm{Tr}_{\mathrm{vib}} \, \hat{\rho}$) in a non-perturbative manner. For a target spectral density $\mathcal{J}(\omega)$ of the physical model that one wants to simulate, the equivalence between the unitary dynamics of $\hat{H}$ with a continuous distribution of harmonic oscillators and the non-unitary dynamics of the pseudomode model with a single damped oscillator relies on matching the correlation function $\mathcal{C}(t)$ of the environment in Eq. (8)

[79, 80]. We note that an anti-symmetrized Lorentzian spectral function is required to satisfy the property of vanishing coupling at zero energy $\mathcal{J}(0) = 0$, which stems from thermodynamic constrains [89]. This would require using more than a single pseudomode to properly fit the anti-symmetrized Lorentzian. Nonetheless, when a single Lorentzian function is located at high-frequency, this only leads to negligible artifacts and electronic and vibronic resonances are still well resolved. We refer to Ref. [72] for a full analysis with numerically exact simulations.

C. Quantum Algorithm

For a model with N sites, N qubits are used to simulate the electronic subspace and N further qubits to add damped oscillators (pseudomodes). Our quantum circuits simulate the closed model in Fig. 1 **a** with $\gamma = 0$ using Trotterized quantum evolution on the quantum computer and 10^4 shots per time step. Our model-specifc error-mitigation scheme, which based on discarding shots from the raw measurement results, filters out sources of noise like depolarization that are incompatible with the pseudomode formalism while retaining damping in the hardware qubits. The quantum computer will then exhibit an effective damping rate $\Gamma_{\mathrm{QC}} > 0$ that is strongly influenced by the qubits with the worst properties in the circuit, such as short coherence time and large gate errors (see Fig. 1 **b**). Note that we attempt to reach the longest possible lifetime by choosing the qubits with the best properties, instead of targeting a specific damping rate.

1. Trotterized Dynamics

We perform a Trotter expansion of the time-evolution operator of the full Hamiltonian in Eq. (1) over time $t_m = m \, \Delta t$,

$$e^{-\mathrm{i}\hat{H}m\Delta t} \approx \left[e^{-\mathrm{i}\hat{H}_{\mathrm{el}}\Delta t} \, e^{-\mathrm{i}\hat{H}_{\mathrm{vib}}\Delta t} \, e^{-\mathrm{i}\hat{H}_{\mathrm{el-vib}}\Delta t} \right]^m. \quad (11)$$

For all our simulations on the quantum computer, we evolve an initial excitation in the donor site with a fixed time step $\Delta t = 4 \, \mathrm{fs}$. This value represents a good compromise between total circuit depth and Trotter error and is motivated by the fact that the highest frequency in our Hamiltonian (Eq. (1)) is around $(11 \, \mathrm{fs})^{-1}$, stemming from the large Coulomb binding energy $V = 2420 \, \mathrm{cm}^{-1}$ of bound electron-hole pairs in organic molecules.

To validate the Trotter approximation, we compare to classical simulations with a smaller time step of $\Delta t = 0.5 \, \mathrm{fs}$ in App. B.

2. Quantum Circuits and Qubit Encoding

The quantum circuit corresponding to a single Trotter step is outlined in Fig. 3 a. The gates can be organized in four parallel layers, such that the circuit depth does not grow when increasing the number of sites N.

For problem sizes with more than $N = 3$ sites $(3 + 3$ qubits), an additional layer of parallelized SWAP gates has to be introduced when mapping the model to the heavy-hex layout processor of IBM_AACHEN (see Fig. 1 b for $N = 7$). While the mapping onto the heavy-hex topology is already very efficient, even shorter circuits with no SWAP gates and therefore longer time evolution are possible for quantum computers with a square topology. An efficient routing strategy to scale up the number of sites in such a case is illustrated in Fig. 3 b

We encode N nearest-neighbor coupled electronic sites on a chain of N qubits, where measuring a qubit in state $|1\rangle$ means localization of an electron at the corresponding site. The N quantum oscillators are truncated after the first excited state (involving $N_b = 2$ levels) and each oscillator is mapped onto a single qubit by identifying the number operator with the Pauli $\hat{Z}$ operator and the displacement operator with Pauli $\hat{X}$. As explained in Sec. II B, this truncation is motivated by the fact that high-frequency modes cannot be thermally activated. The model can easily be extended with more levels per oscillator or the addition of more pseudomodes, as shown in App. C 1 together with the explicit qubit mapping.

Although models with more complex vibrational structures are outside the scope of this work, it is also possible to include more oscillators as shown in Fig. 3 c, where the number of qubits per oscillator should reflect their expected populations. Crucially, modes participating in vibronic coherences should be assigned as close as possible to their corresponding site qubit. The involved gates, scaling complexity and hardware execution times of the circuits are discussed in more detail in App. C 2.

3. Quantum Noise

We assume that noisy processes in the hardware stem from two major sources. On the one hand, amplitude damping and pure dephasing are continuously affecting all qubits, even if they are idle. On the other hand, imperfections in the hardware implementation of single and two-qubit gates introduce depolarising noise that progressively destroys quantum coherence among qubits. After mapping the full Hamiltonian Eq. (1) to operators acting on qubits in the processor, we model hardware noise with a master equation within the Lindbladian formalism

$$\mathcal{L}(\hat{\rho}) = \sum_{n,\alpha} \gamma_{n,\alpha} \left(\hat{L}_{n,\alpha}\, \hat{\rho}\, \hat{L}_{n,\alpha}^\dagger - \frac{1}{2} \{ \hat{L}_{n,\alpha}^\dagger\, \hat{L}_{n,\alpha}, \hat{\rho} \} \right), \quad (12)$$
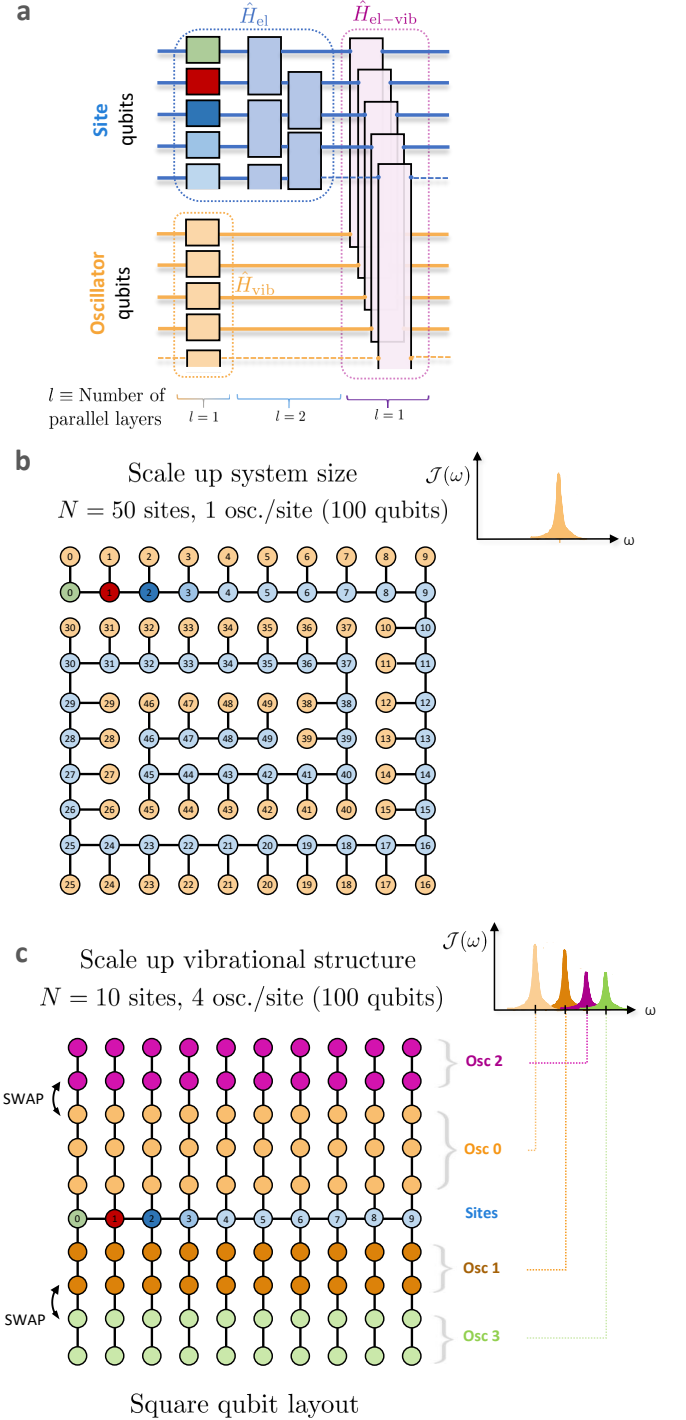

FIG. 3. **Circuit structure and routing strategy for large-scale simulations on square qubit layouts. a.** Quantum circuit corresponding to a single Trotter step, consisting of four parallelisable layers. The vibronic coupling term $\hat{H}_{\mathrm{el-vib}}$ in magenta consists of parallelized two-qubit entangling gates between site qubits and their corresponding oscillator qubit. **b.** Vibronic models with a single oscillator per site can be scaled up without increasing circuit depth. The example shows a model with $N = 50$ sites (100 qubits) on a 10×10 square layout processor. **c.** When scaling up the vibrational structure by adding multiple oscillators per site, the local vibrational environment of site n can be encoded in the upper/lower rows at the n-th column.

Lindblad op. $\hat{L}_{n,\alpha}$	Type of Noise	Site qubits	Osc. qubits
$\hat{\sigma}_{n,\alpha}^{-}$	Amp. Damping	$\times$	$\checkmark$
$\hat{\sigma}_{n,\alpha}^{z}$	Pure Dephasing	$\times$	$\checkmark$
$\hat{\sigma}_{n,\alpha}^{x}, \hat{\sigma}_{n,\alpha}^{y}, \hat{\sigma}_{n,\alpha}^{z}$	Depolarization	$\times$	$\times$

TABLE I. **Sources of hardware noise that are compatible with the pseudomode formalism.** Amplitude damping and pure dephasing acting on oscillator qubits can be exploited to engineer the target damping rate of pseudomodes. Noise acting on qubits that are used to encode electronic sites have no correspondence in our target model and hence need to be fully mitigated.

where the operators $\hat{L}_{n,\alpha}$ refer to noise processes acting on the n-th qubit, and the α index distinguishes between different noise processes. As summarised in Tab. I, we exploit the intrinsic amplitude damping of the qubits that are used to realize damped oscillators (pseudomodes) in Eq. (10) on the quantum processor. Because amplitude damping also introduces dephasing, pure dephasing acting on oscillator qubits can also be properly accommodated by considering an effective damping rate that depends on the T_1, T_2 times of each particular qubit [51]. Furthermore, pure dephasing on qubits assigned to electronic sites can be identified with a constant offset in the spectral density [51], although this already constitutes a deviation from our target model. We refer to App. C3 for more details. Note that other noise processes are detrimental and need to be mitigated (see next subsection).

For any experiment of Trotterized dynamics on the quantum computer, the correspondence between hardware error rates and the effective damping rate Γ_{QC} that one is able to simulate depends on the hardware execution time $T_{\mathrm{exec}}^{\mathrm{Trot.}}$ of one Trotter circuit and the particular choice of simulation time step [51], which we fixed to Δt=4 fs for all our experiments on the quantum computer. After selecting qubits that are connected by low gate errors that are comparable to each other, a reasonable lower bound for the effective damping rate Γ_{QC} is given by

$$\Gamma_{\mathrm{QC}} \gtrsim \frac{T_{\mathrm{exec}}^{\mathrm{Trot.}}}{\Delta t} \frac{1}{\min_q(T_1^{(q)}, T_2^{(q)})} \qquad (13)$$

where $\min_q(T_1^{(q)}, T_2^{(q)})$ refers to the smallest T_1 or T_2 time among the qubits in the circuit.

For selecting suitable hardware qubits in the processor we use Mapomatic [90], where most emphasis is given on finding configurations of qubits with the lowest amount of gate errors (single and two-qubit entangling gates) and low readout error. Among such configurations, we choose T_1, T_2 times that are as large as possible. We reserve the best qubits for encoding electronic sites, since only noisy oscillator qubits are compatible with our model (see Tab. I). Nonetheless, we find that gate fidelities and the minimum of the T_1, T_2 times are the main limiting factor for accurate simulations when encoding either sites or oscillators in the quantum processor. We refer to App. C4 for further details about our criteria to select suitable qubit layouts.

4. Error Mitigation

To enable accurate simulations over many time steps while retaining a meaningful damping rate, we need to suppress other sources of noise that are incompatible with the target model insofar as possible. Entangling gates in superconducting processors introduce for example strong depolarising noise that tends to equilibrate the populations of all qubits. We process the readout error mitigated [91] data and employ two levels of model-specific error mitigation, enabling long time evolution. First, we discard shots that do not comply with particle conservation in the electronic subsystem ($\sum_{n=0}^{N-1} \hat{a}_n^{\dagger} \hat{a}_n = 1$ in $\hat{H}_{\mathrm{el}}$), since the creation or annihilation of electronic excitations is not possible in the Hamiltonian model (Eq. (1)). This particle conservation constitutes a powerful error mitigation strategy at the post-processing stage that is crucial for long-time evolution [87].

Secondly, we set a limit to the maximum number of vibrational excitations ($\sum_{n=0}^{N-1} \hat{b}_n^{\dagger} \hat{b}_n \leq 1$ in $\hat{H}_{\mathrm{vib}}$), as the total energy in the system is usually around at most $2\omega_0$ and spreads over all electronic sites and all oscillators. As schematically shown in the right panel of Fig. 2**b**, vibronic resonances are driven by the entanglement between electronic states and quantized vibrations, forming non-separable superpositions of zero and one-phonon configurations. For this reason, we only keep shots with a small number of vibrational quanta. Note that the number of vibrational quanta should not be limited for models with oscillators that can be thermally activated, nevertheless, extensions to the pseudomode formalism with coupled oscillators can accurately reproduce nonzero temperatures while initialising all oscillators to their ground state, regardless of their frequencies [79]. The accuracy of our results could be enhanced by techniques from classical simulations of open quantum systems like time-adaptive diagonalization in an ever-larger vibrational basis [92] and other efficient multiparticle encodings of large vibronic systems with a few vibrational excitations [93].

When combined with noise characterization and error mitigation techniques like randomized compiling and probabilistic error cancellation, partial control over error rates in the qubits can be achieved [52]. Nevertheless, there is a limit to the extent that unwanted sources of noise can be filtered out from the raw data.

5. Emulation and Classical Simulation

To validate the performance of our quantum simulations, we compare against two different types of numerical simulations in this work. We refer to simulations

of the quantum circuits ($\Delta t = 4\,\text{fs}$, $N_b = 2$) as *emulations*. They involve no noise besides amplitude damping on qubits encoding oscillators and are obtained with the QuEST toolkit [94]. Simulations of the target model using a smaller time step $\Delta t = 0.5\,\text{fs}$ and $N_b = 5$ levels per oscillators are referred to as *classical simulations* and obtained using the Dissipation-Assisted Matrix Product Factorization (DAMPF) method, which efficiently applies the pseudomode approach in tensor networks. [79, 85]. While the comparison to emulations allows us to assess the effects of noise in the quantum computer, classical simulations can be considered an exact benchmark with negligible Trotter error and negligible truncation error from oscillators (see App. B for further details).

III. RESULTS AND DISCUSSION

We have performed quantum dynamics simulations of the one-dimensional donor-acceptor model with vibronic coupling on the IBM_AACHEN Heron processor, for problem sizes ranging from $N = 3$ Sites (6 qubits) up to $N = 10$ (20 qubits) in total, where each oscillator is mapped to a single qubit. We first show the capabilities of our approach by probing different electron transfer mechanisms, and in the second part discuss the scaling behaviour with respect to the problem size N.

A. Probing Electronic and Vibronic Transfer Mechanisms with $N = 5$ Sites ($5 + 5$ Qubits)

We evolve an initial excitation in the donor site and aim for a qualitative reproduction of the time-averaged probability of electron transfer $P_{\text{transfer}}(\Delta, T)$,

$$P_{\text{transfer}}(\Delta, T) = \frac{1}{T} \sum_{n=2}^{N} \int_0^T P_n(t)\mathrm{d}t, \qquad (14)$$

as a function of the driving force Δ and integration time T, where $P_n(t)$ is the population of site n. The transfer probability describes the probability of an electron moving from the donor to the acceptor without getting stuck in the trap, see Fig. 2 a. We expect two types of peaks in $P_{\text{transfer}}(\Delta, T)$, associated with the electronic and vibronic mechanism of ET illustrated in Fig. 2 b.

In Fig. 4 a we show error-mitigated experimental results for the site population dynamics $P_n(t)$ on IBM_AACHEN at an electronic resonance with driving force $\Delta_e = 1435\,\text{cm}^{-1}$ for the case without vibronic coupling ($g = 0$). For comparison, the lower panel shows the classical simulation (using $\Delta t = 0.5\,\text{fs}$). We observe both slow and fast modulations of the population in time. The slow modulations stem from the superposition of a pair of eigenstates of the electronic Hamiltonian $\hat{H}_{\text{el}}$ that arise from the mixing of donor-acceptor states when the donor is resonant with an eigenstate of the acceptor subsystem,

as schematically shown in Fig. 2 b. The fast modulations correspond to an energy gap around Δ_e, indicating a contribution of the ground state near $-V$ to the superposition. We refer to App. A for a detailed analysis of the states participating in the mechanisms of electronic and vibronic ET.

In Fig. 4 b we show $P_{\text{transfer}}(\Delta, T)$ resulting from simulations with different Δ after $T = 75$ fs and $T = 200$ fs (18 and 50 time steps). We compare quantum simulations without vibronic coupling ($g = 0$ in Eq. (4)) using 5 qubits for the sites and simulations incorporating vibronic coupling ($g > 0$) to local oscillators using 5+5 qubits for sites and oscillators. The structure of P_{transfer} is well reproduced and the peaks are revealed at the expected driving forces. The quantum hardware is able to resolve the vibronic resonance at $\Delta_v = 3010$ cm^{-1} for the case of vibronic coupling ($g > 0$), which only starts to build up after a few vibrational cycles of ≈ 22 fs and continues to rise within the lifetime of vibrational excitation. This is evident when comparing $P_{\text{transfer}}(75\,\text{fs})$ with $P_{\text{transfer}}(200\,\text{fs})$. An artifact of depolarising noise is that P_{transfer} is raised in an artificial manner, because it tends to equilibrate the populations of all qubits. These artifacts are most prominent in regions where neither electronic nor vibronic resonances are present, leading to an overestimation of P_{transfer}, as seen for example around $\Delta = 2000\,\text{cm}^{-1}$ in $P_{\text{transfer}}(200\,\text{fs})$. The existing noise in the quantum hardware will therefore set a limit to the maximum time that one can integrate the probability of transfer while revealing structure, rather than adding a global shift in P_{transfer}. The electronic resonance shown in Fig. 4 a is marked with a red cross at Δ_e, while the vibronic resonance case shown in Fig. 4 c is indicated in red markers at Δ_v.

In Fig. 4 c we show the population dynamics $P_n(t)$ of the quantum simulations with driving force Δ_v and compare them in the bottom panel to classical simulations ($\Delta t = 0.5$ fs, $N_b = 5$) with a damping rate of $(112.5\,\text{fs})^{-1}$, which we identified as the effective damping rate Γ_{QC} with the lowest deviation between our quantum simulation and classical simulations with rates ranging from $(12.5\,\text{fs})^{-1}$ to $(500\,\text{fs})^{-1}$ (see App. D). The dynamics showcases the slow build-up of populations at sites $n = 2$ and $n = 4$ in the case of vibronic coupling (right), while the excitation stays localized at the donor in the case of no coupling (left). This confirms that vibronic coupling is behind this mechanism by entangling electronic eigenstates with oscillator excitations. Maintaining the contrast in P_{transfer} between $g = 0$ and $g > 0$ at vibronic resonances is the basis for our proposal to use microscopic ET as an application-based benchmark.

In Fig. 4 d we show the evolution of populations $P_n(t)$ at the vibronic resonance $\Delta_v = 3010$ cm^{-1} in the presence of vibronic coupling ($g > 0$). We show the raw experimental data (black crosses) and after error mitigation (orange circles), demonstrating the impact of our model-specific mitigation protocol. While the raw data exhibits a fast equalization of the populations of all qubits,
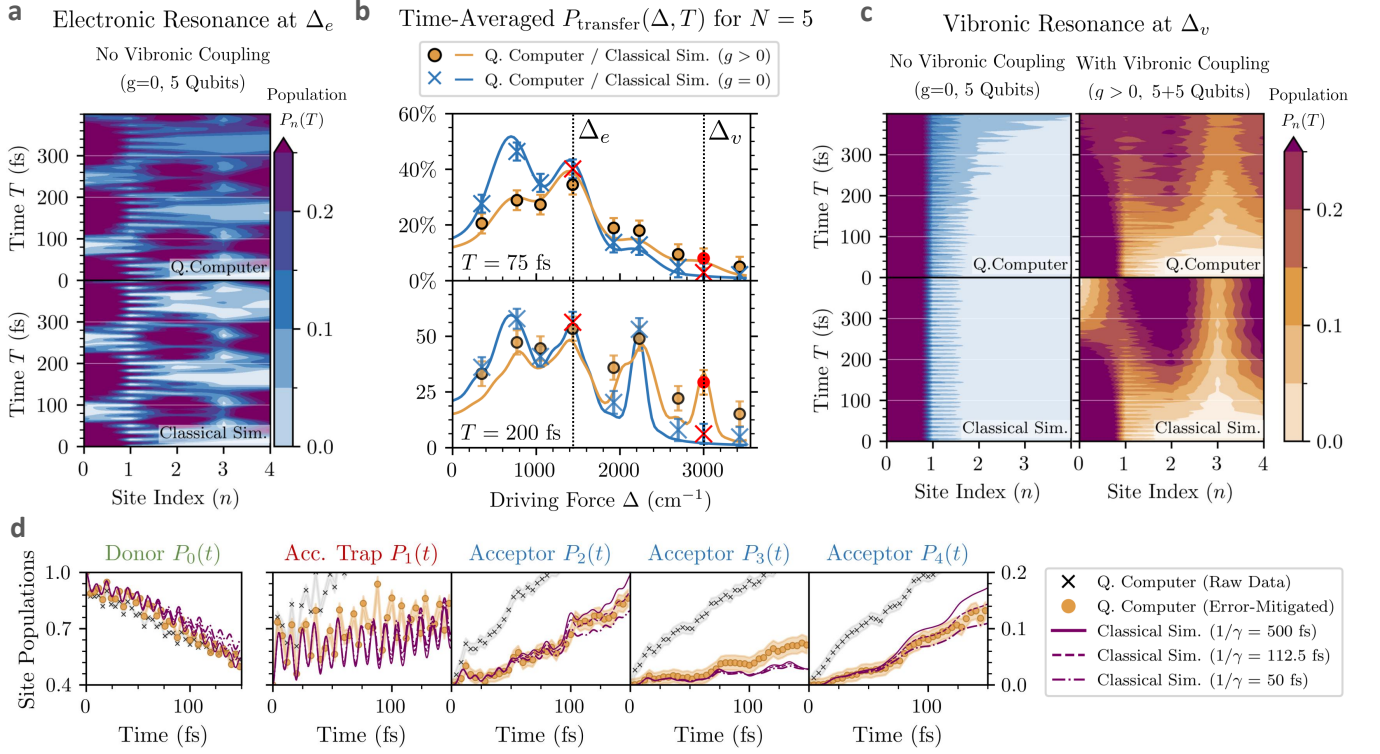
FIG. 4. **Probing different charge transfer mechanisms for** $N = 5$ **sites on** IBM_AACHEN. **a.** The top panel shows a quantum simulation of the population dynamics $P_n(t)$ for an electronic resonance at $\Delta_e = 1435\,\text{cm}^{-1}$ without vibronic coupling ($g = 0$) on 5 qubits. The bottom panel shows a classical simulation ($\Delta t = 0.5\,\text{fs}$) for reference. **b.** Transfer probability $P_{\text{transfer}}(\Delta, T)$ (see Eq. (14)) for $T = 75\,\text{fs}$ (top panel) and $T = 200\,\text{fs}$ (bottom panel) for the cases with ($g > 0$ in orange, 10 qubits) and without ($g = 0$ in blue, 5 qubits) vibronic coupling. The points show expectation values obtained from the experiment, with error bars accounting for shot noise. The curves display classical simulations with a damping rate of $\gamma = (500\,\text{fs})^{-1}$. The simulations shown in **a** and **c** are marked in red. **c.** The top panels shows a quantum simulation of the population dynamics $P_n(t)$ at the vibronic resonance ($\Delta_v = 3010\,\text{cm}^{-1}$) without ($g = 0$, blue) and with ($g > 0$, orange) vibronic coupling. The bottom panels show classical simulations ($\Delta t = 0.5\,\text{fs}$, $N_b = 5$) of the target model with a damping rate of $(112.5\,\text{fs})^{-1}$ as reference. **d.** Population dynamics $P_n(t)$ of the run with Δ_v and $g > 0$ (also shown in **c**) with and without error mitigation, and three classical simulations with increasing damping rates. Each time point corresponds to a unique quantum circuit sampled with 10^4 shots.

error-mitigated data is well matched to classical simulations. We show three classical simulations with increasing damping rates of $(500\,\text{fs})^{-1}$ (solid lines), $(112.5\,\text{fs})^{-1}$ (dashed lines) and $(50\,\text{fs})^{-1}$ (dashed-dotted lines). We note how the highly damped simulation shows a stronger increase of the trap population, while the weakly damped system has a more effective electron transfer to the acceptor sites. The periodic pumping of population from the donor to acceptor sites gives rise to a *ratchet*-like growth of the populations $P_2(t), P_3(t), P_4(t)$, along with the quenching of population on the acceptor trap $P_1(t)$. These are signatures of a quasi-stationary, nonequilibrium state that provides ultrafast vibronic ET and is sustained within the lifetime of vibrational excitations. The populations $P_2(t)$, $P_4(t)$ on the quantum computer lie within the populations of the two classical simulations with the largest and the weakest damping rate, and the effective damping rate Γ_{QC} of the quantum computer must lie within $(50\,\text{fs})^{-1} - (500\,\text{fs})^{-1}$. Interestingly, the

populations $P_n(t)$ of the sites with the largest contribution to this vibronic resonance ($n = 2$ and $n = 4$) are better reproduced than the population of *spectator* sites like $n = 3$, whose population stays relatively low and it is overestimated on the quantum computer (see App. A for a detailed analysis of the eigenstates involved at this resonance).

We find that effective damping rates Γ_{QC} can vary substantially between different runs of the same experiment, for a systematic assessment we refer to App. D. Nonetheless, our analysis shows that Γ_{QC} is mostly determined by the quality of entangling gates and the lowest T_1, T_2 times of qubits on the quantum circuit.

B. Scaling Up the Number of Sites

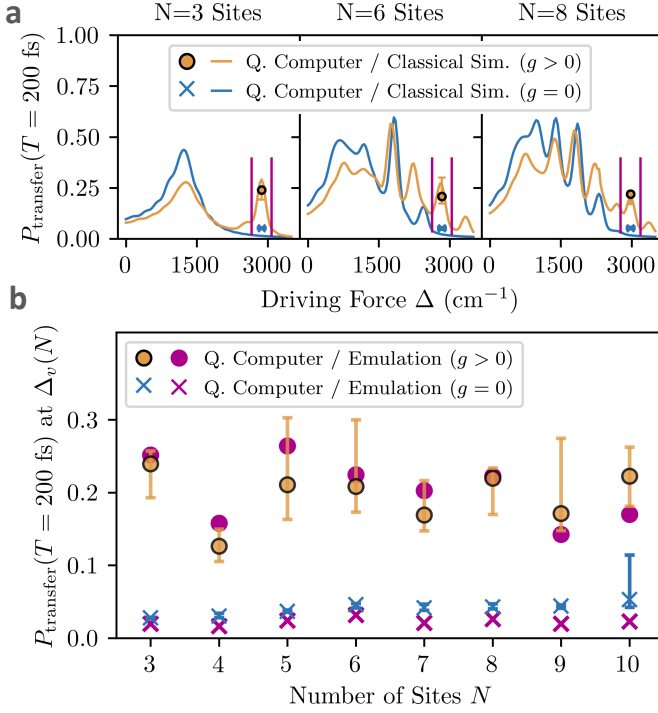In this section we probe the capacity of the quantum computer to scale up the problem size N by simulating

FIG. 5. **Probability of vibronic ET for increasing number of sites.** For each system size N we show experimental results for $P_{transfer}(T = 200\,fs)$ obtained from 10 different quantum simulations on IBM_AACHEN for the case with vibronic coupling ($g > 0$) on up to 20 qubits, and 3 different quantum simulations without vibronic coupling ($g = 0$) on up to 10 qubits. The orange circles (blue crosses) show the median transfer probability for $g > 0$ ($g = 0$), while the error bars indicate the smallest and largest value. **a.** We show the experimental results for $N = 3, 6$ and 8 over the driving force Δ, together with classical simulations ($\Delta t = 0.5\,fs$, $N_b = 5$). The vertical lines in magenta indicate the vibronic peaks which we chose for our quantum simulations. **b.** We show experimental results over the number of sites N, compared against noiseless emulations ($\Delta t = 4\,fs$, $N_b = 2$). Note that the height varies between vibronic peaks due to the changing energy landscape.

vibronic resonances from $N = 3$ sites up to $N = 10$ on IBM_AACHEN. We simulated the population dynamics with vibronic coupling ($g > 0$) on 10 different days using 6 to 20 qubits, and the case without vibronic coupling ($g = 0$) on 3 different days using 3 to 10 qubits. In Sec. III B 1 we investigate the resulting transfer probabilities, then we discuss the performance and error of our simulations in Sec. III B 2 by comparing to emulations and classical simulations, and at last we show scalability of our error mitigation technique in Sec. III B 3.

1. Resolving Vibronic Transfer Probabilities

The vibronic mechanism of ET relies on non-separable states where electronic sites and oscillators are entangled, as shown in Fig. 2 **b** and in more detail in App. A. This way, our simulations of vibronic resonances will test the ability of the quantum processor to maintain entangled bipartitions of sites and oscillators over a considerable number of time steps until population starts to build up in the acceptor site. To validate our proposal of ET simulations as an application-based benchmark, we simulate ET with vibronic coupling ($g > 0$) on $N + N$ qubits and compare with the case without vibronic coupling ($g = 0$) on N qubits at the same driving force, where ET is surpressed. The constant depth of the Trotter circuits thereby ensures comparability while increasing the problem size N.

In Fig. 5 we show experimental results for the transfer probability $P_{transfer}(\Delta_v, T)$ after $T = 200\,fs$ (50 time steps) for system sizes ranging from $N = 3$ to $N = 10$ using up to 20 qubits. The orange circles (blue crosses) give the median value for $P_{transfer}$ of the 10 (3) simulations for $g > 0$ ($g = 0$), while the error bars indicate the lowest and highest result. As shown Fig. 5 **a**, the energy landscape and the structure of vibronic resonances change with the problem size N, requiring us to carefully select for each N a driving force that corresponds to a genuine vibronic resonance. The specific driving forces $\Delta_v(N)$ for each N are given in App. B.

In Fig. 5 **b** we compare the experimental results for different system sizes N against noiseless emulations. For every case, we obtained at least one run with very strong agreement to the emulation when using $N + N$ qubits in the presence of vibronic coupling $g > 0$. In the absence of vibronic coupling, the experimental values using N qubits lie even closer to the emulated values, and the probability of transfer at $\Delta_v(N)$ gets suppressed when $g = 0$. The variance of experimental results across independent runs is significantly larger for $g > 0$ ($N + N$ qubits) than for $g = 0$ (N qubits). We attribute this to the availability of a sufficiently large set of connected qubits with low error rates, which is fluctuating between days for the used device. This is also illustrated by the outlier for $g = 0$ and $N = 10$, which compared to the simulations for $N \leq 9$ from the same day had to use one additional qubit with considerably worse error rates.

Furthermore, our simulations show good separation between the cases $g = 0$ and $g > 0$ for all system sizes N, verifying that the increase in $P_{transfer}$ was indeed mediated by vibronic coupling and entangled site-oscillator states in the quantum processor, instead of being a product of depolarising noise.

2. Comparison Against Numerical Simulations

In this section we investigate the accuracy of our quantum simulations when increasing the amount of electronic
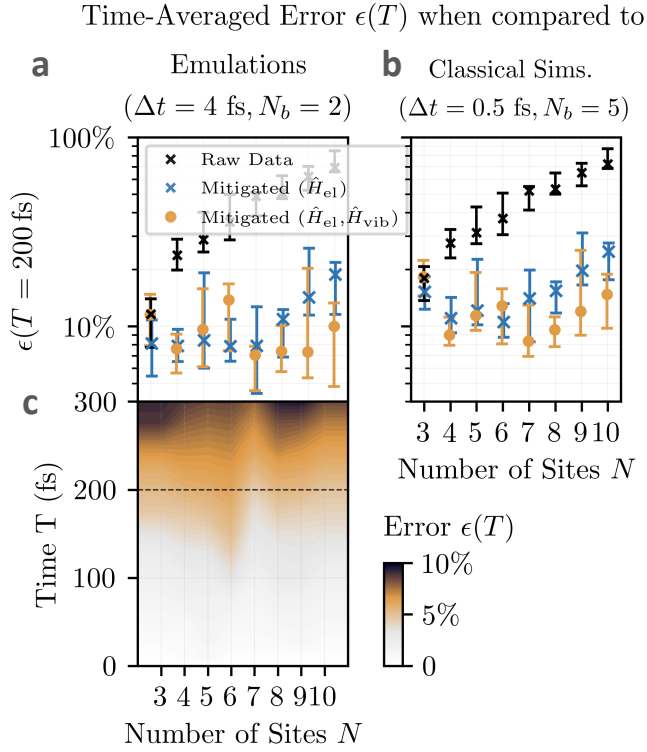
Time-Averaged Error $\epsilon(T)$ when compared to

a Emulations $(\Delta t = 4\,\text{fs}, N_b = 2)$ **b** Classical Sims. $(\Delta t = 0.5\,\text{fs}, N_b = 5)$

FIG. 6. **Time-averaged error $\epsilon(T)$ against the weakly damped target model $(\gamma = (1\,\text{ps})^{-1})$ for different levels of error mitigation. a.** Comparison against emulations $(\Delta t = 4\,\text{fs}, N_b = 2$ levels per oscillator). **b.** Comparison against classical simulations $(\Delta t = 0.5\,\text{fs}, N_b = 5)$. **c.** Heatmap showing the simulation error $\epsilon(T)$ compared against the emulations, as a function of the total evolution time T of the fully mitigated results, whereby for each N and T the run with the lowest error is shown. The time corresponding to the errors shown in **a** and **b** is indicated with a dashed line.

sites and qubits, and with respect to the number of time steps. For this reason, we compare our experiments on the quantum computer against emulations and classical simulations of our target model. We choose a target damping rate of $\gamma = (1\,\text{ps})^{-1}$, corresponding to long-lived system-bath correlations that are considered challenging for conventional computers due to their demand in memory. We define the simulation error

$$\epsilon(T) = \sum_t \frac{\sqrt{\sum_n |P_n(t) - P_n^{(\text{ref.})}(t)|^2}}{T}. \qquad (15)$$

with respect to the populations of the electronic system sites $P_n^{(\text{ref.})}(t)$ calculated with a reference method, either emulations $(\Delta t = 4\,\text{fs}, N_b = 2)$ or classical simulations $(\Delta t = 0.5\,\text{fs}, N_b = 5)$. Note that this deviation from these reference calculations can also correspond to accurate dynamics with a stronger effective damping rate $\Gamma_{\text{QC}} > \gamma = (1\,\text{ps})^{-1}$ (see Fig. 14 in App. D).

Because the hardware properties of superconducting processors may significantly vary on the time scale of several hours, 10 independent experiments were executed

on IBM_AACHEN for each system size N across different days. The circuits corresponding to the last three days were transpiled with a variable-angle, single-qubit R_X gate, leading to shorter circuits and a better performance overall. The circuits corresponding to the remaining days were transpiled with fixed-angle single-qubit SqrtX gates. We refer to App. C 3 for a full comparison between these two cases.

In Fig. 6 **a** we show the minimum, maximum and median $\epsilon(T)$ in Eq. (15) of all ten data points at $T = 200\,\text{fs}$ for each N for the case with vibronic coupling $(g > 0)$ and the different levels of error mitigation, when comparing to emulations $(\Delta t = 4\,\text{fs}, N_b = 2)$. As expected, discarding data points that violate the conservation of site excitations improves the site population dynamics. Discarding measurements with more than a single vibrational excitation further improves the accuracy of population dynamics overall. Remarkably, the lowest error $\epsilon(T)$ achieved for any of these simulations is for $N = 7$ (7+7 qubits). This fits to the hardware calibration data, as the qubit properties over multiple days are found to be best on average for $N = 7$, and further the experimental run for $N = 7$ with the lowest error corresponds to the experiment with the best qubit properties, in particular the highest minimum T_1, T_2 times and lowest gate errors (see Fig. 12 in App. C 4 for the calibration data between different runs).

In Fig. 6 **b** we show the same analysis when comparing against classical simulations $(\Delta t = 0.5\,\text{fs}, N_b = 5)$. Due to the smaller time step and larger number of oscillator levels, these reference calculations exhibit negligible Trotter and oscillator truncation errors, making both errors visible in $\epsilon(T)$ when comparing the quantum simulations $(\Delta t = 4\,\text{fs}, N_b = 2)$. Therefore, all quantum simulations show higher $\epsilon(T)$ compared to Fig. 6 **a**, but the same trend, as Trotter and truncation error do not grow with the system size N (see App. B). In particular, the experimental run for $N = 7$ still has the best accuracy of all simulations. Note that for $N = 3$, mitigation of the site qubits lowers the error, while oscillator mitigation leads to higher error because it discards processes with two vibrational excitations, which have a larger impact in small system sizes.

In Fig. 6 **c** we plot the time evolution of the error $\epsilon(T)$ with respect to emulations, showing for each system size N and time point T the fully mitigated experimental data with the lowest error. Surprisingly, the error does not increase with the system size N. This is consistent with the fact that we obtained for every N at least one very accurate simulation, and with our observation that the accuracy of quantum simulations only depends on the availability of a sufficiently large connected set of good qubits. We observe slowly increasing deviation from the undamped dynamics as the simulation time increases, reaching a time-averaged error of 10% after around 300 fs, indicating the current limit in simulation time.
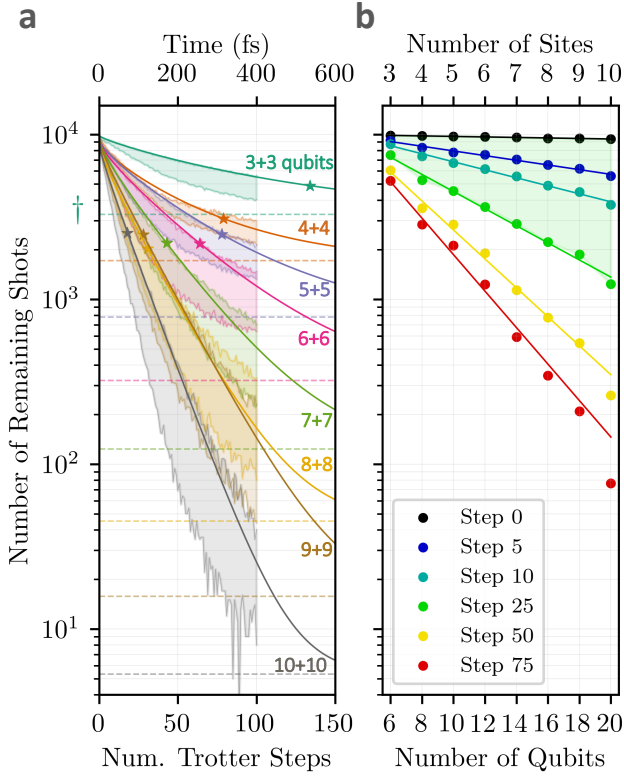
FIG. 7. **Amount of shots remaining after error mitigation. a.** Number of remaining shots as a function of the number of Trotter steps (1 step $\equiv \Delta t=4$ fs), after discarding measurements corresponding to unphysical states with more than two vibrational excitations. For each system size $N = 3 - 10$, the shaded area indicates the highest and lowest number of shots among the ten independent simulations with vibronic coupling ($g > 0$). The dashed horizontal lines refer to the expected number of shots if the processor is in the completely mixed state, marked with a dagger for $N = 3$ (6 qubits). The solid lines correspond to a numerical fit (Eq. (16)), interpolating between a power law and an exponential decay towards the completely mixed state, with this transition indicated with star markers. **b.** Remaining number of shots as a function of the number of qubits evaluated at increasing number of Trotter steps ($0 - 300$ fs). The solid lines correspond to a numerical fit with an exponential decay (Eq. (17)). The green area indicates the largest Trotter step for which the total execution time lies within the lowest T_1, T_2 times of qubits in the circuit ($\sim 30\,\mu s$ for $N_{\text{qubits}} \leq 16$ and $\sim 10\,\mu s$ for $N_{\text{qubits}} = 20$).

3. Scalability of Error Mitigation

As discussed in Sec. II C 4, we apply error mitigation as a post-processing method by discarding shots from the raw measurements that do not comply with particle conservation in the electronic subsystem ($\sum_{n=0}^{N-1} \hat{a}_n^\dagger \hat{a}_n = 1$ in $\hat{H}_{\text{el}}$). Furthermore, we set a limit to the number of vibrational excitations ($\sum_{n=0}^{N-1} \hat{b}_n^\dagger \hat{b}_n \leq N_{\text{max}}$ in $\hat{H}_{\text{vib}}$). While we chose $N_{\text{max}} = 1$ for all results presented above,

the analysis of remaining shots in this subsection here chooses $N_{\text{max}} = 2$, motivated by the fact that states with two vibrational excitations participate to a small extent in the charge transfer process for the smallest system sizes ($N = 3$ or $N = 4$), ensuring that all discarded shots are truly stemming from errors. Nonetheless, it is worth noting that the choice of N_{max} depends on the structure of the vibrational environment and the energy of the initial state.

While error mitigation drastically increases the amount of time steps for which the simulation stays accurate, the number of shots s available to compute expectation values after mitigation is an important consideration, as the error with respect to shot noise when measuring populations scales as $\epsilon_{\text{shot-noise}} \sim \frac{1}{\sqrt{s}}$ per observable. Furthermore, the spread of the site population over an increasing number of sites may lead to smaller fluctuations in each site, requiring a higher precision. Scaling up the system size therefore demands measuring more shots as time evolves for more accuracy but also due to the error mitigation overhead.

In Fig. 7 a we show the number of remaining shots as a function of the number of time steps. As a reference we plot in dashed lines for each problem size N the number of shots $s_{N,\text{mixed}} = N(1+N+\binom{N}{2})/4^N$ that would remain if the quantum processor was in the completely mixed state, not containing any information. We observe that for many time steps, the number of remaining shots is decaying towards this bound.

A possible explanation for the loss of shots with increasing number of time steps are the different types of noise occurring on the hardware. Over the first time steps, we find a power-law behavior that we attribute to gate infidelities. This power-law decay is stronger for more qubits, corresponding to the increasing average gate errors as shown in Tab. II. After enough time steps, we find that the loss of shots transitions from power-law to exponential. This happens when the execution time of the circuit on the hardware approaches the regime of the smallest T_1 and T_2 times involved in the circuit, indicating the effect of continuous noise. To test this claim, we fitted for each N the simple model

$$s_N(t; \tau, a, b) = s_N(t = 0)p_{\text{valid}}(t; \tau, a, b) \quad (16)$$
$$+ s_{N,\text{mixed}}\, p_{\text{mixed}}(t; \tau, a, b),$$
$$p_{\text{valid}}(t; \tau, a, b) = (1 - at^b)e^{-t/\tau},$$
$$p_{\text{mixed}}(t; \tau, a, b) = 1 - e^{-t/\tau},$$

to the quantum simulation with the largest number of remaining shots $s_N(t)$ at the end of the simulation ($t = 400$ fs). Notably, the parameter τ (indicated with star markers in Fig. 7 a) marks the transition from the power-law behavior of gate error propagation to the exponential scaling of damping and dephasing noise, and is indeed in good agreement with the lowest T_1, T_2 times when considering the circuit execution times in Tab. III. In particular, the transition occurs twice as late for $N = 3$, the only case where no SWAP gates are required, reflecting

that the corresponding circuit execution time is half as long as for $N > 3$.

In Fig. 7 b we show the number of remaining shots as a function of the number of qubits at specific time steps. The solid lines at each Trotter step were obtained with a numerical fit

$$s_{\text{Step}}(N_{\text{qubits}}; C, r) = C \, e^{-r N_{\text{qubits}}} \tag{17}$$

with prefactor C and rate r. While the number of remaining shots has a exponential dependence with the total number of qubits N_{qubits}, the rate r is highly dependent on the number of time steps. For steps 0, 5, 10, 25, 50 and 75 we find $1/r$ values of 278, 31, 18, 8, 5 and 4 respectively, indicating at each Trotter step, the number of qubits for which the number of remaining shots is around $1/e$ of its initial value. The values of the prefactor C in Eq. (17) stay close to the initial number of shots in our experiments (10^4) until 25 Trotter steps, while they almost double for 50 steps, indicating the scaling becomes worse than exponential after 25 steps ($T = 100\,\text{fs}$). The execution time of circuits for 25 steps coincides with the lowest T_1, T_2 values in the circuit, illustrating again the importance of the minimum qubit coherence time. We are optimistic the improvement in quantum hardware will therefore enable the simulation of much larger system sizes.

IV. CONCLUSIONS

In this paper we described and tested a procedure to simulate the nonequilibrium dynamics of an open quantum system on a noisy quantum computer, in particular, the vibronically assisted electron-transfer (ET) of a one-dimensional donor-acceptor model. Exploiting the intrinsic damping of hardware qubits and post-processing the raw data with a model-specific error-mitigation scheme, we reproduced vibronic ET using up to 100 Trotter steps for model sizes ranging from $N = 3$ sites (3+3 qubits) to $N = 10$ sites (10+10 qubits). This approach opens an unconventional avenue in quantum computing for the design of new hardware where quantum processors make use of native bosonic elements with parametrizable damping rates, like the motion of trapped ions and superconducting resonators [61–63, 65, 66].

Our experiments on the quantum computer demonstrate its capacity to engineer arbitrary energy landscapes (Ω_n) in extended systems with multiple interacting sites and vibronic coupling to local environments. The formalism can be generalized to engineer arbitrarily complex environments by adding more oscillators, while the depth of the Trotter circuit is independent from the system size N. Although the circuits can be efficiently mapped onto the heavy-hex topology of the IBM_AACHEN device, which we used for our experiments, even shorter circuits can be achieved for processors with a square topology.

We find that the main bottleneck for large-scale simulations is the limited number of qubits that are connected by high-fidelity gates and whose coherence times remain above the threshold set by the target open quantum system that one wants to simulate. While it is technologically feasible to simulate models with arbitrarily high damping rates by artificially amplifying a particular type of noise, the fundamental challenge still lies in the simulation of target models with very low damping rates, requiring qubits with increased coherence times and access to gates with higher fidelities.

We are able to resolve accurately the peak structure of the time-averaged probability of ET transfer as a function of the driving force P_{transfer}, because the accuracy of individual populations are less relevant for spectral-dependent like P_{transfer}, similar to the success of shadow spectroscopic techniques [95]. Nonetheless, simulating spectroscopic experiments would require the measurement of coherences, complicating the scaling of simulations [96].

Long-lived correlations on the picosecond scale are industrially relevant for the design of new energy materials but these Non-Markovian effects are notoriously challenging to simulate with classical techniques. Because the vibronic mechanism is driven by the entanglement between electronic sites and oscillators, the simulation of vibronic ET for increasingly large problem sizes constitutes an application-based benchmark that measures the capacity of the quantum computer to sustain and scale up long-lived entangled states between well defined bipartitions of the processor.

Finally, our error mitigation techniques at the post-processing stage were crucial to filter out unwanted noise from the raw experimental data, making it more compatible with the target open quantum sytem. This allows us to discard shots that do not preserve particle conservation and it could be enhanced with other techniques that may take advantage of the finite speed at which entanglement spreads in the model. The underlying strategy here is to exploit the natural growth of correlations in system-environment frameworks, where a factorized initial state is generally assumed. Experimental results could be improved further by finely-tuned calibration setups at the pre-processing stage, optimizing gates to excel at simulating a particular Hamiltonian parametrization of the target model. This could also be exploited to identify known problems in superconducting qubits such as Two-Level-System artifacts [97].

Appendix A: Electronic and Vibronic Electron Transfer

In Fig. 8 we show in detail the mechanisms of electronic and vibronic ET for the simulations for $N = 5$ sites that were presented in Sec. III A in the main text.

Electronic resonances occur when the donor has similar energy to an eigenstate of the acceptor subsystem $\hat{H}_{\mathrm{el}}^{(\mathrm{Acc.})}$, leading to the superposition of electronic states with a mixed donor-acceptor character, as highlighted in a box in the left panel of Fig. 8. The resulting dynamics will show a slow modulation that is caused by the interference between these two eigenstates, as demonstrated in Sec. III A. The result in Fig. 4 b also shows fast modulations, which can be explained by the interference of these states with the ground state near $-V$ localised at the trap, which shows a small contribution of the initial donor site ($n = 0$) in Fig. 8.

Vibronic resonances occur when the donor energy Ω_0 is far-off from any acceptor states. Vibronic coupling is required in order to produce superpositions of the localized donor with delocalised acceptor states, which takes place if the energy difference is matched by the energy ω_0 of a vibrational excitation. For this reason, the charge transfer at vibronic resonances is driven by the entanglement between electronic states and quantized vibrations, forming non-separable superpositions of zero and one-phonon configurations.

In Fig. 9 we show for each system size N the classically simulated transfer probabilities over the driving force, as well as for each N the driving force at which we simulate vibronic resonances. For a system of N sites there are $N - 2$ vibronic resonances, of which we selected resonances with driving forces much higher than all electronic resonances, to ensure a purely vibronic mechanism.

Appendix B: Numerical Benchmarks and Validity of Approximations

We use two types of numerical benchmarks: Emulations ($\Delta t = 4\,\mathrm{fs}$, $N_b = 2$ levels per oscillator) and clas-
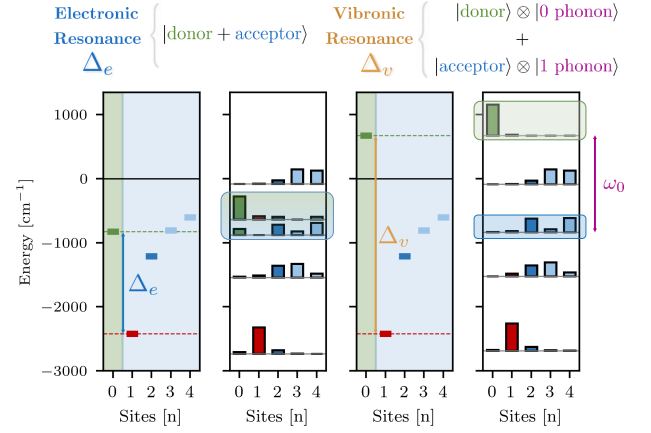

FIG. 8. **Mechanisms of purely electronic and vibronic ET for $N = 5$.** The left subpanels show the energies of the electronic Hamiltonian term $\hat{H}_{\mathrm{el}}$ in site basis, while the right subpanels show its eigenenergies, with the amplitude of each site plotted on top of the bar. At $\Delta_e = 1435\,\mathrm{cm}^{-1}$ (left-hand side), the donor Ω_0 is resonant with the second eigenstate of the acceptor-only electronic subsystem in Eq. (7), producing a superposition of states with mixed donor/acceptor character. At $\Delta_v = 3010\,\mathrm{cm}^{-1} \approx \Delta_e + \omega_0$ (right-hand side), vibronic coupling is required in order to produce superpositions of the localized donor with delocalised acceptor states.

sical simulations ($\Delta t = 0.5\,\mathrm{fs}$, $N_b = 5$). Classical simulations represent the exact dynamics, as we chose the time step Δt and the number of oscillators N_b such that both Trotter and oscillator truncation error become negligible. Hence, comparing the classical simulations to the emulations gives insights about the impact of both Trotter and truncation error together. In this Appendix we also consider a variation of classical simulations with less oscillator levels ($\Delta t = 0.5\,\mathrm{fs}$, $N_b = 2$), such that comparing them against emulations shows the Trotter error, and comparing them against the classical simulation with $N_b = 5$ shows the truncation error.

All three comparisons are shown in Fig. 10, demonstrating that the time-averaged error $\epsilon(T)$ is independent of the system size N for simulation times of 150 fs. For longer evolution times, the Trotter error can become more pronounces for smaller system sizes. The truncation error of oscillators decreases with system sizes, especially when considering long evolution times. For large models with $N > 4$, vibronic resonances with multiple vibrational excitations are less probable, and the vibrational dynamics tend to stay within the subspace of a single vibrational excitation that is coherently shared among all oscillators.

In Fig. 9 we further confirm this analysis by showing the qualitative structure of $P_{\mathrm{transfer}}(\Delta)$ for classical simulations with both $N_b = 2$ and $N_b = 5$ levels per oscillator, validating our quantum simulations with $N_b = 2$.
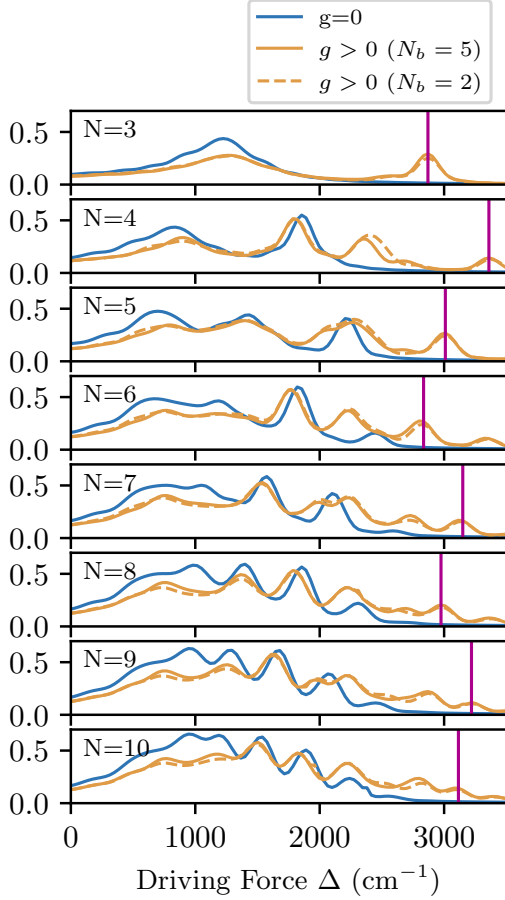
FIG. 9. **Time-averaged probability of electron transfer** $P_{\text{transfer}}(T = 200 \text{ fs})$ **as a function of the driving force for** $N = 3 - 10$ **sites.** We show classical simulations for the case without vibronic coupling ($g = 0$, blue) and with vibronic coupling ($g > 0$, orange, bold). We also show a classical simulation with less levels per oscillator $N_b = 2$ (orange, dashed) to assess the truncation error. The vertical purple bars indicate the driving forces of the respective vibronic peaks that were chosen for the simulations in this work.

Appendix C: Details about Hardware Implementation

1. Qubit Mapping

We map N nearest-neighbor coupled electronic sites directly on a chain of N site qubits $\hat{\sigma}_n$ in the processor as

$$\hat{H}_{\text{el}} \rightarrow \sum_{n=0}^{N-1} \frac{\Omega_n}{2} \hat{\sigma}_n^z + \sum_{n=0}^{N-2} \frac{J}{2} \left(\hat{\sigma}_n^x \hat{\sigma}_{n+1}^x + \hat{\sigma}_n^y \hat{\sigma}_{n+1}^y \right). \quad \text{(C1)}$$

For our LVC Hamiltonian model of electron transfer, we have considered a single oscillator per site ($M_n = 1$ in $\hat{H}_{\text{vib}}$). This allows us to drop the m index in Hamiltonian terms $\hat{H}_{\text{vib}}$ and $\hat{H}_{\text{el-vib}}$ in Eqs. (3) and (4), respec-
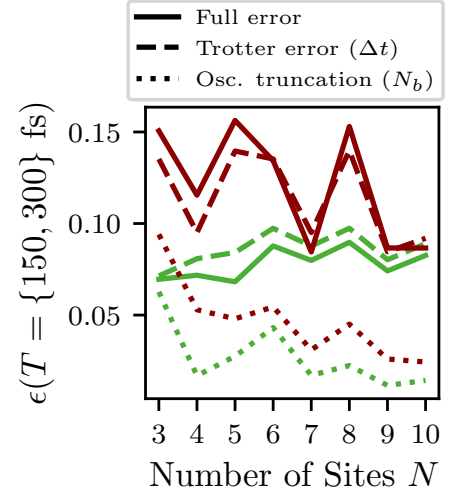

FIG. 10. **Scaling analysis for different approximations contributing to the time-averaged error** $\epsilon(T)$. The difference between emulations ($\Delta t = 4 \text{ fs}$, $N_b = 2$) and classical simulations ($\Delta t = 0.5 \text{ fs}$, $N_b = 5$) includes errors with respect to the the Trotter approximation and the oscillator truncation, and is shown in bold. We compare both benchmarks against a variation of classical simulation with ($\Delta t = 0.5 \text{ fs}$, $N_b = 2$), which allows to isolate the Trotter error (dashed) and truncation error (dotted). We show the errors for $T = 150 \text{ fs}$ (green) and $T = 300 \text{ fs}$ (brown).

tively. Each local quantum harmonic oscillator in the LVC Hamiltonian is then identified by its index n and mapped onto an arbitrary number of Q oscillator qubits in the quantum computer. We replace each of the $\hat{b}_n^\dagger \hat{b}_n$ bosonic operators in (3), and coupling operators $\hat{b}_n^\dagger + \hat{b}_n$ in (4), by a sum of Q oscillator qubit operators $\hat{\sigma}_{n,q}$ such that

$$\hat{b}_n^\dagger \hat{b}_n \rightarrow \sum_{q=0}^{Q-1} \hat{\sigma}_{n,q}^+ \hat{\sigma}_{n,q}^-,$$

$$\hat{b}_n^\dagger + \hat{b}_n \rightarrow \frac{1}{\sqrt{Q}} \sum_{m=0}^{Q-1} \hat{\sigma}_{n,q}^x. \quad \text{(C2)}$$

This boson-to-qubit mapping introduces an error $\mathcal{O}(1/Q)$ [51] and is better suited for low excitation numbers. The vibrational part of the Hamiltonian is mapped onto qubits as

$$\hat{H}_{\text{vib}} \rightarrow \sum_{n=0}^{N-1} \sum_{q=0}^{Q-1} \omega_n \hat{\sigma}_{n,q}^+ \hat{\sigma}_{n,q}^-, \quad \text{(C3)}$$

and the vibronic coupling term describing the interaction between the electronic states and oscillators is mapped onto qubits as

$$\hat{H}_{\text{el-vib}} \rightarrow \sum_{n=0}^{N-1} \sum_{q=0}^{Q-1} g_n \left(\hat{\sigma}_n^z \otimes \hat{\sigma}_{n,q}^x \right). \quad \text{(C4)}$$

	$N = 3$ (6 qubits)			$N = 10$ (20 qubits)		
Property	Min	Median	Max	Min	Median	Max
1Q-Gate Error	1.1e-4	1.8e-4	2.9e-4	1.0e-4	2.0e-4	1.09e-3
2Q Gate Error	1.5e-3	1.8e-3	2.7e-3	1.2e-3	1.9e-3	5.9e-3
T_1 Sites	136 µs	218 µs	315 µs	108 µs	218 µs	333 µs
T_1 Osc.	175 µs	211 µs	274 µs	73 µs	175 µs	344 µs
T_2 Sites	167 µs	255 µs	331 µs	77 µs	211 µs	349 µs
T_2 Osc.	184 µs	218 µs	330 µs	46 µs	189 µs	349 µs
Readout Error	2.9e-3	3.6e-3	4.8e-3	2.3e-3	4.7e-3	1.84e-2

TABLE II. Calibration data of those qubits in IBM_AACHEN that were used for the simulations of population dynamics of the smallest and largest model with $N = 3, 10$ sites, averaged over all 10 simulations on different days.

2. Quantum Circuits

The circuit corresponding to a single time step Δt in a first-order Trotter decomposition of the time-evolution operator $\hat{\mathcal{U}}(t) = e^{-i\hat{H}t}$ is schematically shown in Fig. 3 a. The blue box $\hat{H}_{\text{el}}$ deploys N single-qubit rotations to encode the individual energies Ω_n of system qubits and then, nearest-neighbors interactions with coupling strength J are natively corresponding to a series of $N-1$ R$_{\text{XX}}$ and R$_{\text{YY}}$ gates, which on IBM_AACHEN are implemented with two CZ gates and single-qubit rotations. The odd and even terms can be executed in parallel. The orange box ($\hat{H}_{\text{vib}}$) commutes with $\hat{H}_{\text{el}}$ and can be executed in parallel using N single-qubit rotations only. Finally, the magenta vibronic coupling term ($\hat{H}_{\text{el-vib}}$) can be done with a parallel cascade of N R$_{\text{XZ}}$ gates, implemented on IBM_AACHEN with two CZ gates and single-qubit rotations, entangling each of the system qubits with their corresponding environment qubit. The number of entangling gates, depth and gate execution times depending on the system size N is given in Tab. III.

As illustrated in Fig. 1 b, for the experiment on real hardware, we had to adapt the quantum circuits to the heavy-hex qubit layout of Heron processors: the chain of sites and their attached oscillators is split into groups of three. We use two SWAP gates per Trotter step to connect each of the $\lfloor N/3 \rfloor$ pairs of separated sites. Note that the pairs of SWAP gates can be executed in parallel, such that the circuit depth does not increase with the problem size N. This enables scaling up to arbitrary system sizes.

3. Quantum Noise

The hardware noise processes we aim to exploit for the simulation of our target model are continuous noise
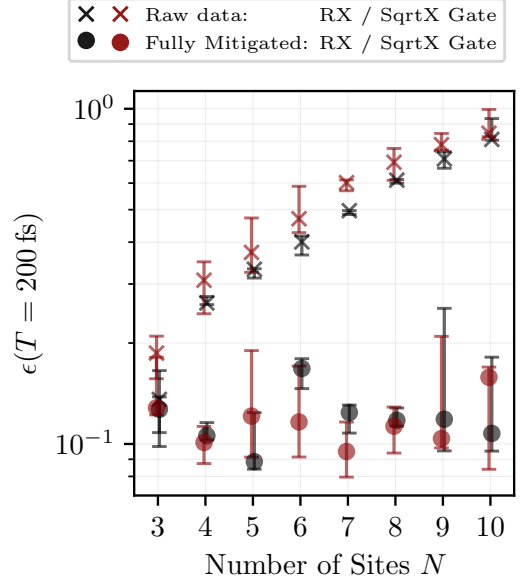

FIG. 11. **Comparison of experimental results with fixed-angle SqrtX vs. variable-angle R_X single qubit gates.** Circuits were compiled with two different types of native gates (both groups of simulations together make up the data presented in Fig. 6 a). The median, largest and smallest of each simulation error $\epsilon(T = 200 \text{ fs})$ is shown for the unprocessed and the fully mitigated date, compared to emulations ($\Delta t = 4$ fs, $N_b = 2$)

processes and are described by a Lindblad superoperator

$$\mathcal{L}(\hat{\rho}) = \sum_{n,\alpha} \gamma_{n,\alpha} \left(\hat{L}_{n,\alpha} \, \hat{\rho} \, \hat{L}_{n,\alpha}^{\dagger} - \frac{1}{2} \{ \hat{L}_{n,\alpha}^{\dagger} \, \hat{L}_{n,\alpha}, \hat{\rho} \} \right). \tag{C5}$$

The operators $\hat{L}_{n,\alpha}$ refer to noise processes acting on the n-th qubit, and the α index distinguishes between different noise processes. In Tab. I we give an overview which processes can be exploited for our target model.

In order to determine the effective noise occurring over one Trotter time step, we have to analyze the impact of noise after every gate in the Trotter circuit $\mathcal{U}_{\text{trot}}$. We model the effect of both continuous noise and gate noise together as a non-unitary operation N_j occurring locally after the execution of each idle operation or gate G_j [49] on the involved qubits. The effective hardware noise can be obtained by moving all noise operations to the right side of the Trotter circuit to occur after all gates, using commutation relations and the small angle approximation, introducing perturbed noise operations N_j':

$$\mathcal{U}_{\text{trot}} = G_1 G_2 \cdots G_k \longrightarrow G_1 N_1 G_2 N_2 \cdots G_k N_k$$
$$\approx G_1 G_2 \cdots G_k N_1' N_2' \cdots N_k. \tag{C6}$$

The perturbation of noise operations from N_j to N_j' are stronger, the larger the rotation angle of a gate is, and the larger the amplitude of the noise operation. This means

# Qubits	Layers SWAPs	Total # CZ gates	Compiled with R_X			Compiled with $\sqrt{X}$			Fit parameters Fig. 7 (all fits to R_X)	
			Depth 1Q	Depth Total	$T_{\text{exec.}}^{\text{Trot.}}$	Depth 1Q	Depth Total	$T_{\text{exec.}}^{\text{Trot.}}$	$\text{Min}(T_1, T_2)$ [µs]	Time step (τ)
6	0	10	12	18	0.6 µs	24	30	0.8 µs	68	134 (80 µs)
8	2	20	20	32	1.2 µs	36	48	1.5 µs	95	79 (95 µs)
10	2	24	20	32	1.2 µs	36	48	1.5 µs	87	78 (94 µs)
12	2	28	20	32	1.2 µs	36	48	1.5 µs	87	64 (77 µs)
14	2	38	20	32	1.2 µs	36	48	1.5 µs	35	43 (52 µs)
16	2	42	20	32	1.2 µs	36	48	1.5 µs	63	31 (37 µs)
18	2	46	20	32	1.2 µs	36	48	1.5 µs	35	28 (34 µs)
20	2	54	20	32	1.2 µs	36	48	1.5 µs	35	18 (22 µs)

TABLE III. **Circuit properties of a single Trotter step.** For each number of sites N and corresponding number of qubits $2N$ we display the circuit depth, number of layers of SWAP-Gates, the total number of CZ-Gates and the estimated execution time on IBM_AACHEN, based on execution times of 32 ns for single-qubit-gates and 68 ns for the CZ-gate. We did simulations using the variable-angle RX-Gate and using the SqrtX-Gate. The latter case shows longer execution times, because usually two SqrtX express one RX-Gate.

that for example the effective action of pure amplitude damping noise may be altered when using large angle gates, and is an important consideration in circuit design.

Hence, generally speaking, small-angle rotation gates should be preferred over large-angle gates like SqrtX or CNOT. To test this claim, we compiled the same circuits to either the large-angle SqrtX gate or the small (variable) angle Rx gate. A direct comparison in Fig. 11 shows lower errors compared to using variable angle Rx gates when considering the raw data, however after error-mitigation we find a tendency of the runs using SqrtX gates to show lower errors on average. Note that we compare here against emulations with $\gamma = (1\,\text{ps})^{-1}$, and that a higher error for runs using Rx gates can be caused by closer alignment to a simulation with damping rate γ as shown in App. D.

4. Criteria for Qubit Selection

For selecting the hardware qubits on which we place the qubit Hamiltonian, we use Mapomatic [90] to filter the sets of qubits on IBM_AACHEN with the lowest error accumulated over all single-qubit and two-qubit gates involved in the circuit. The best of these sets are then evaluated for their T_1 (damping) and T_2 (dephasing) times. We found that good simulation results are ensured if the T_1 and T_2 times of all qubits are above a certain threshold of around $50 - 100$ times the execution time of one Trotter time step. If this requirement is difficult to fulfill while maintaining good gate fidelities, then a set is picked where all system-qubits have a sufficiently large T_1, T_2 times, and then when at least all SWAP-qubits are sufficient. Averaged calibration data of the noise model of the qubits used on IBM_AACHEN for the smallest and largest model $(N = 3, 10)$ are given in Tab. II, showing that indeed the availability of qubits with sufficiently large T_1, T_2 times is less for larger systems. For the simulation presented here, the median properties for both

$N = 3$ and $N = 10$ are similar, however the qubit set for $N = 10$ has some noisy outliers, affecting the overall simulation accuracy. Readout errors of the average qubit were sufficiently low to have a weak impact on the results. Our focus is the simulation of long-time evolution with as many time steps as possible (i.e circuit depth), rather than the measurement of populations very accurately at all times.

In Fig. 12 we show the variation of calibration data, in **a** for $N = 7$ (14 qubits) between different runs, and in **b** between different system sizes N. The most accurate simulations where performed with $N = 7$, corresponding to the simulation with the largest minumum T_1, T_2 in the circuit and lowest single-qubit and two-qubit errors, validating our qubit selection scheme.

Appendix D: Effective Hardware Damping Rates

This appendix discusses the effective damping rate Γ_{QC} of our experimental results after the post-processing, stemming from intrinsic hardware noise that was not filtered by error mitigation. We compare our results on the quantum computer with classical simulations ($\Delta t = 0.5\,\text{fs}$, $N_b = 5$) of the target model with different fixed damping rates γ, ranging from $(12.5\,\text{fs})^{-1}$ to $(500\,\text{fs})^{-1}$.

In Fig. 13 **a** we compare the experimental results on the quantum computer for $N = 5$ at the vibronic resonance against classical simulations with three damping rates of $(500\,\text{fs})^{-1}$, $(112.5\,\text{fs})^{-1}$ and $(50\,\text{fs})^{-1}$. In Fig. 13 **b**, we plot the time-averaged error $\epsilon(T)$ between the experimental result and classical simulations with variable damping rates. The lowest error at $T = 200\,\text{fs}$ is achieved for an effective damping rate $\Gamma_{\text{QC}} = (112.5\,\text{fs})^{-1}$. Although the population dynamics of acceptor sites are better matched to $\Gamma_{\text{QC}} = (112.5\,\text{fs})^{-1}$, we note how the population of the donor site $P_0(t)$ exhibits a slower decay.

In Fig. 14 we show this comparison for $N = 7$ sites for two simulations performed on different days. Panel
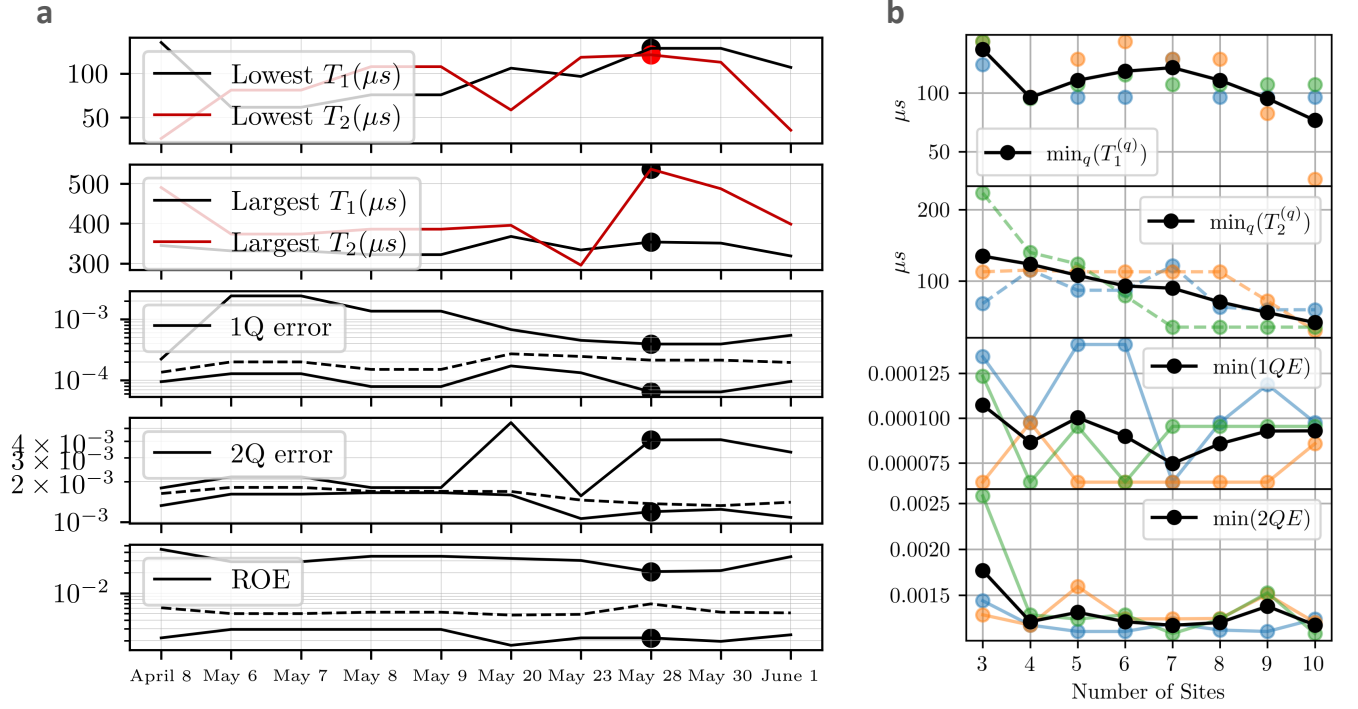
FIG. 12. **Variability of calibration data between different days for the simulations using** $N = 7$ **sites (14 qubits).**
a. We show the minimal and maximal T_1, T_2 times of all involved qubits, and the minimum, median and maximum for the single- and two-qubit fidelities and for the readout error. The calibration of the simulation with the lowest error $\epsilon(T)$ is marked with a point. **b.** For the last three days utilizing variable-angle, single-qubit R_x gates, qubit properties are shown as a function of the number of sites N ($N + N$ qubits). Colored markers correspond to the three individual runs, while averaged quantities are shown in black.
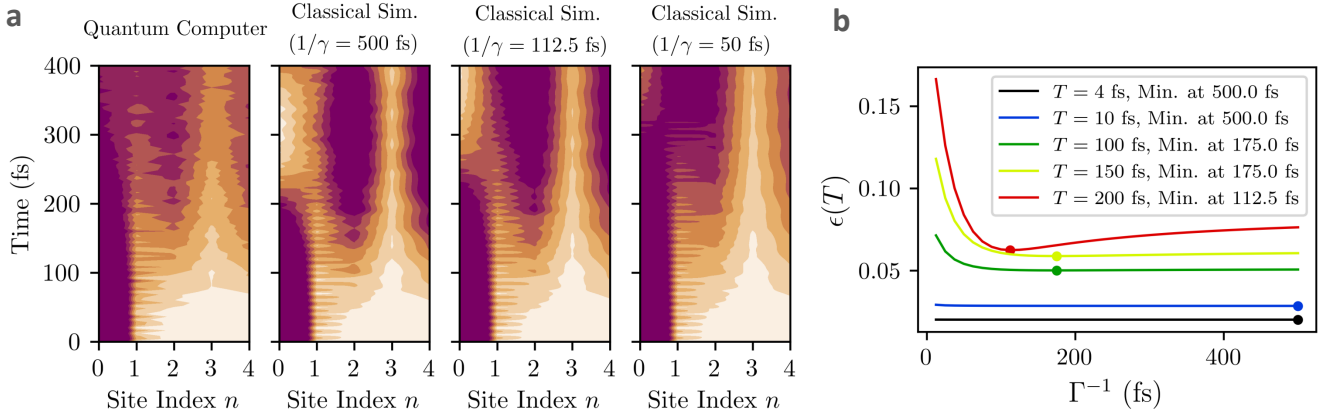

FIG. 13. **Extracting effective damping rate** Γ_{QC} **for** $N = 5$. **a.** Population dynamics at the vibronic resonance for $N = 5$ sites (5+5 qubits) executed on IBM_AACHEN on May 28, 2025, compared against classical simulations with three different damping rates. **b.** Time-averaged error $\epsilon(T)$ between experimental results and classical simulations with a fixed damping rate γ, plotted for $T = 4, 10, 100, 150$ and 200 fs. The minimum errors are marked with a dot each.

a shows the explicit dynamics of two different days compared to classical simulations with those damping rates that yielded the smallest time-averaged error $\epsilon(T)$ after $T = 300$ fs. Panel **b** shows the time-averaged error $\epsilon(T)$ for $T = 150$ fs and 300 fs when varying γ. While the simulations from May 7 appears closest to an undamped model after 150 fs, but with more simulation time approaches a damped behaviour with a rate of $(137.5\,\text{fs})^{-1}$. The simulation from May 28 appears more strongly damped behaviour over the whole simulation time, with rates ranging between $(62.5\,\text{fs})^{-1}$ and $(87.5\,\text{fs})^{-1}$. Note that the resembles the ideal case, as the
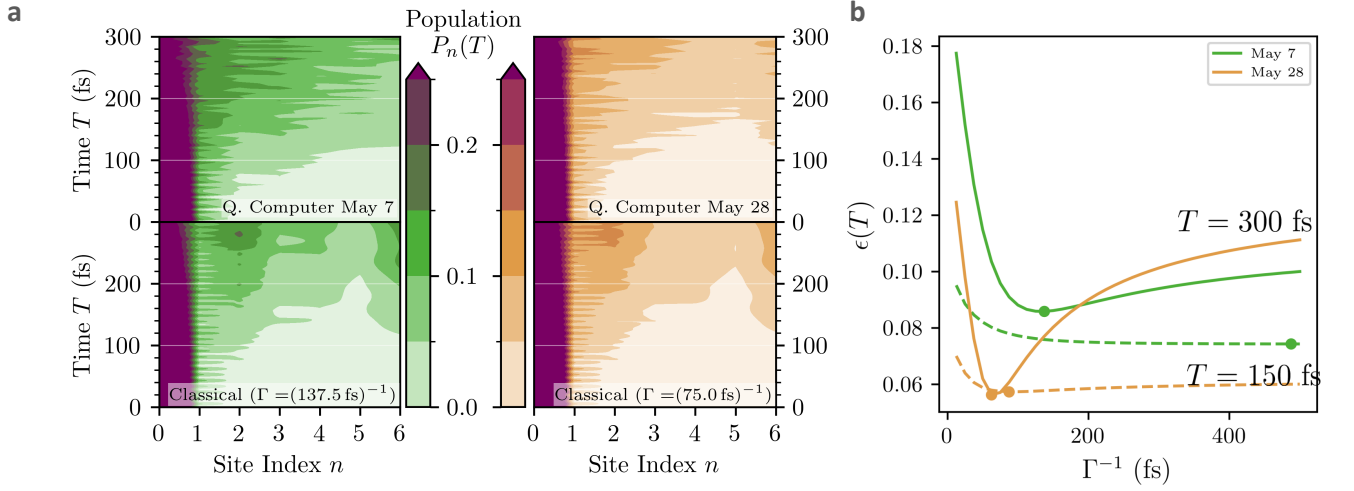
FIG. 14. **Variability between independent experimental results and their corresponding effective damping rate** Γ_{QC}. **a.** Population dynamics at the vibronic resonance for $N = 7$ sites (14 qubits) executed on IBM_AACHEN on May 7, 2025 and May 28, 2025, compared against classical simulations. Note that the run on May 7 uses SqrtX gates while May 28 uses the variable-angle Rx gate. **b.** Time-averaged error $\epsilon(T)$ between experimental results and classical simulations with a fixed damping rate γ, plotted for $T = 150\,\text{fs}$ (dashed) and $T = 300\,\text{fs}$ (bold) over γ. The minimum errors are marked with a dot each.

time-averaged error does not increase over time and has its minimum always in a small region around $(75\,\text{fs})^{-1}$.

[1] R. Naaman, D. H. Waldeck, and J. Fransson, New Perspective on Electron Transfer through Molecules, The Journal of Physical Chemistry Letters **13**, 11753 (2022).

[2] J. Wang, T. Ding, K. Gao, L. Wang, P. Zhou, and K. Wu, Marcus inverted region of charge transfer from low-dimensional semiconductor materials, Nature Communications **12**, 6333 (2021).

[3] D. Fraggedakis, M. McEldrew, R. B. Smith, Y. Krishnan, Y. Zhang, P. Bai, W. C. Chueh, Y. Shao-Horn, and M. Z. Bazant, Theory of coupled ion-electron transfer kinetics, Electrochimica Acta **367**, 137432 (2021).

[4] G. A. Parada, Z. K. Goldsmith, S. Kolmar, B. Pettersson Rimgard, B. Q. Mercado, L. Hammarström, S. Hammes-Schiffer, and J. M. Mayer, Concerted proton-electron transfer reactions in the Marcus inverted region, Science **364**, 471 (2019).

[5] H. Oberhofer, K. Reuter, and J. Blumberger, Charge Transport in Molecular Materials: An Assessment of Computational Methods, Chemical Reviews **117**, 10319 (2017).

[6] N. J. Williams, R. E. Warburton, I. D. Seymour, A. E. Cohen, M. Z. Bazant, and S. J. Skinner, Proton-coupled electron transfer at SOFC electrodes, The Journal of Chemical Physics **158**, 244107 (2023).

[7] H. Cheng, Q. Sun, L. Li, Y. Zou, Y. Wang, T. Cai, F. Zhao, G. Liu, Z. Ma, W. Wahyudi, Q. Li, and J. Ming, Emerging Era of Electrolyte Solvation Structure and Interfacial Model in Batteries, ACS Energy Letters **7**, 490 (2022).

[8] P. Benedek, N. Yazdani, H. Chen, N. Wenzler, F. Juranyi, M. Månsson, M. S. Islam, and V. C. Wood, Surface phonons of lithium ion battery active materials, Sustainable Energy & Fuels **3**, 508 (2019).

[9] R. B. Smith and M. Z. Bazant, Multiphase Porous Electrode Theory, Journal of The Electrochemical Society **164**, E3291 (2017).

[10] P. Bai and M. Z. Bazant, Charge transfer kinetics at the solid–solid interface in porous electrodes, Nature Communications **5**, 3585 (2014).

[11] M. Z. Bazant, Theory of Chemical Kinetics and Charge Transfer based on Nonequilibrium Thermodynamics, Accounts of Chemical Research **46**, 1144 (2013).

[12] N. Lorenzoni, T. Lacroix, J. Lim, D. Tamascelli, S. F. Huelga, and M. B. Plenio, Full Microscopic Simulations Uncover Persistent Quantum Effects in Primary Photosynthesis (2025), arXiv:2503.17282 [physics].

[13] C. Giannetti, C. , Massimo, F. , Daniele, F. , Michele, P. , Fulvio, , and D. Mihailovic, Ultrafast optical spectroscopy of strongly correlated materials and high-temperature superconductors: a non-equilibrium approach, Advances in Physics **65**, 58 (2016).

[14] C.-H. Cheng and P.-Y. Lai, Theory of nonequilibrium asymptotic state thermodynamics: Interacting Ehrenfest urn ring as an example, Physical Review E **108**, 064114 (2023).

[15] V. A. Mikhailova and A. I. Ivanov, Effect of Relaxation of Intramolecular High-Frequency Vibrational Mode on Nonthermal Electron Transfer Probability. Stochastic Point-Transition Approach, The Journal of Physical Chemistry C **111**, 4445 (2007).

[16] J.-C. Zheng, X.-W. Zheng, X.-L. Hei, Y.-F. Qiao, X.-Y. Yao, X.-F. Pan, Y.-M. Ren, X.-W. Huo, and P.-B. Li, Non-Markovian dynamics with λ-type atomic systems in a single end photonic waveguide (2025), arXiv:2503.15216 [quant-ph].

[17] Zhi Guo, Yan Wan, Mengjin Yang, Jordan Snaider, Kai Zhu, Libai Huang, Long-range hot-carrier transport in hybrid perovskites visualized by ultrafast microscopy, Science **356**, 59 (2017).

[18] S. Kahmann and M. A. Loi, Hot carrier solar cells and the potential of perovskites for breaking the Shockley–Queisser limit, Journal of Materials Chemistry C **7**, 2471 (2019).

[19] K. K. Nielsen, L. A. P. Ardila, G. M. Bruun, and T. Pohl, Critical slowdown of non-equilibrium polaron dynamics, New Journal of Physics **21**, 043014 (2019).

[20] A. Schirato, M. Maiuri, G. Cerullo, and G. D. Valle, Ultrafast hot electron dynamics in plasmonic nanostructures: experiments, modelling, design, Nanophotonics **12**, 1 (2023).

[21] R. J. Preston, Y. Ke, S. L. Rudge, N. Hertl, R. Borrelli, R. J. Maurer, and M. Thoss, Nonadiabatic Quantum Dynamics of Molecules Scattering from Metal Surfaces, Journal of Chemical Theory and Computation **21**, 1054 (2025).

[22] I. Rahinov, A. Kandratsenka, T. Schäfer, P. Shirhatti, K. Golibrzuch, and A. M. Wodtke, Vibrational energy transfer in collisions of molecules with metal surfaces, Phys. Chem. Chem. Phys. **26**, 15090 (2024).

[23] S. Ghan, E. Diesen, C. Kunkel, K. Reuter, and H. Oberhofer, Interpreting ultrafast electron transfer on surfaces with a converged first-principles Newns–Anderson chemisorption function, The Journal of Chemical Physics **158**, 234103 (2023).

[24] A. Hashemi, P. Peljo, and K. Laasonen, Understanding Electron Transfer Reactions Using Constrained Density Functional Theory: Complications Due to Surface Interactions, The Journal of Physical Chemistry C **127**, 3398 (2023).

[25] I. Lončarić, M. Alducin, J. I. Juaristi, and D. Novko, CO Stretch Vibration Lives Long on Au(111), J. Phys. Chem. Lett. **10**, 1043 (2019).

[26] R. J. V. Wagner, B. C. Krüger, G. Barratt Park, M. Wallrabe, A. M. Wodtke, and T. Schäfer, Electron transfer mediates vibrational relaxation of CO in collisions with Ag(111), Physical Chemistry Chemical Physics **21**, 1650 (2019).

[27] D. Novko, J. Tremblay, M. Alducin, and J. Juaristi, Ultrafast Transient Dynamics of Adsorbates on Surfaces Deciphered: The Case of CO on Cu(100), Phys. Rev. Lett. **122**, 016806 (2019).

[28] A. L. Utz, Vibrations that live long and prosper, Nature Chem **10**, 577 (2018).

[29] D. Novko, M. Alducin, M. Blanco-Rey, and J. I. Juaristi, Effects of electronic relaxation processes on vibrational linewidths of adsorbates on surfaces: The case of CO/Cu(100), Phys. Rev. B **94**, 224306 (2016).

[30] A. Gross and M. Scheffler, Influence of molecular vibrations on dissociative adsorption, Chemical Physics Letters **256**, 417 (1996).

[31] Q. Bian, F. Ma, S. Chen, Q. Wei, X. Su, I. A. Buyanova, W. M. Chen, C. S. Ponseca, M. Linares, K. J. Karki,

A. Yartsev, and O. Inganäs, Vibronic coherence contributes to photocurrent generation in organic semiconductor heterojunction diodes, Nat Commun 11, 617 (2020).

[32] F. Ma, E. Romero, M. R. Jones, V. I. Novoderezhkin, and R. van Grondelle, Both electronic and vibrational coherences are involved in primary electron transfer in bacterial reaction center, Nat Commun 10, 933 (2019).

[33] P. P. M. Schleker, C. Grosu, M. Paulus, P. Jakes, R. Schlögl, R.-A. Eichel, C. Scheurer, and J. Granwehr, Electrolyte contact changes nano-Li4Ti5O12 bulk properties via surface polarons, Communications Chemistry 6, 1 (2023).

[34] S. Ahn, J. Kim, B. Kim, and S. Kim, First-principles study on small polaron and Li diffusion in layered Li-CoO2, Physical Chemistry Chemical Physics 25, 27848 (2023).

[35] H. D. Luong, T. L. Tran, V. B. T. Phung, and V. A. Dinh, Small polaron transport in cathode materials of rechargeable ion batteries, Journal of Science: Advanced Materials and Devices 7, 100410 (2022).

[36] M. Kick, C. Grosu, M. Schuderer, C. Scheurer, and H. Oberhofer, Mobile Small Polarons Qualitatively Explain Conductivity in Lithium Titanium Oxide Battery Electrodes, The Journal of Physical Chemistry Letters 11, 2535 (2020).

[37] M. Kick, C. Scheurer, and H. Oberhofer, Polaron-Assisted Charge Transport in Li-Ion Battery Anode Materials, ACS Applied Energy Materials 4, 8583 (2021), publisher: American Chemical Society.

[38] A. Banday, M. Ali, R. Pandey, and S. Murugavel, Direct evidence for the influence of lithium ion vacancies on polaron transport in nanoscale LiFePO4, Physical Chemistry Chemical Physics 21, 9858 (2019).

[39] Z. Liu, P. B. Balbuena, and P. P. Mukherjee, Hole Polaron Diffusion in the Final Discharge Product of Lithium–Sulfur Batteries, The Journal of Physical Chemistry C 121, 17169 (2017).

[40] G. Tao, Nonequilibrium Electron-Coupled Lithium Ion Diffusion in LiFePO4: Nonadiabatic Dynamics with Multistate Trajectory Approach, The Journal of Physical Chemistry C 120, 6938 (2016).

[41] C. Franchini, M. Reticcioli, M. Setvin, and U. Diebold, Polarons in materials, Nature Reviews Materials 6, 560 (2021).

[42] D. Windsor and H. Xu, Polarons: Energetics and their structural and electronic effects in ATiO₃ perovskite systems, Physical Review Materials 7, 055004 (2023).

[43] D. Bao, Q. Chang, B. Chen, X. Chen, H. Sun, Y. M. Lam, D. Zhao, J.-X. Zhu, and E. E. Chia, Evidence of Polaron Formation in Halide Perovskites via Carrier Effective Mass Measurements, PRX Energy 2, 013001 (2023).

[44] T. L. Britt, F. Caruso, and B. J. Siwick, A momentum-resolved view of polaron formation in materials, npj Computational Materials 10, 1 (2024).

[45] Z. Wang, B. Miglani, S. Yuan, and K. H. Bevan, On the application of Marcus–Hush theory to small polaron chemical dynamics in oxides: its relationship to the Holstein model and the importance of lattice–orbital symmetries, Physical Chemistry Chemical Physics 26, 4812 (2024).

[46] S. McBride, W. Chen, T. Cuk, and G. Hautier, Do Small Hole Polarons Form in Bulk Rutile TiO2?, The Journal of Physical Chemistry Letters , 2333 (2025).

[47] Y. Guo, D. Wu, Z. Sun, F. Ning, K. Zhu, X. Liu, S. Lu, Y. Xia, and J. Yi, The Role of Ion-Polaron Electrostatic Attraction on Zn2+ Migration in α-V2O5 for Zinc Ion Battery: Insights from First-Principles Calculations, The Journal of Physical Chemistry Letters 16, 1415 (2025).

[48] A. Kemper, O. Abdurazakov, and J. Freericks, General Principles for the Nonequilibrium Relaxation of Populations in Quantum Materials, Physical Review X 8, 041009 (2018).

[49] K. R. Fratus, K. Bark, N. Vogt, J. Leppäkangas, S. Zanker, M. Marthaler, and J.-M. Reiner, Describing Trotterized Time Evolutions on Noisy Quantum Computers via Static Effective Lindbladians (2022), arXiv:2210.11371 [quant-ph].

[50] K. R. Fratus, J. Leppäkangas, M. Marthaler, and J.-M. Reiner, The Discrete Noise Approximation in Quantum Circuits (2023), arXiv:2311.00135 [quant-ph].

[51] J. Leppäkangas, N. Vogt, K. R. Fratus, K. Bark, J. A. Vaitkus, P. Stadler, J.-M. Reiner, S. Zanker, and M. Marthaler, Quantum algorithm for solving open-system dynamics on quantum computers using noise, Phys. Rev. A 108, 062424 (2023).

[52] J. D. Guimarães, J. Lim, M. I. Vasilevskiy, S. F. Huelga, and M. B. Plenio, Noise-Assisted Digital Quantum Simulation of Open Systems Using Partial Probabilistic Error Cancellation, PRX Quantum 4, 040329 (2023).

[53] J. D. Guimarães, A. Ruiz-Molero, J. Lim, M. I. Vasilevskiy, S. F. Huelga, and M. B. Plenio, Optimized noise-assisted simulation of the Lindblad equation with time-dependent coefficients on a noisy quantum processor, Phys. Rev. A 109, 052224 (2024).

[54] T. Wang, Z. Zhang, B.-N. Lu, M. Cirio, and Y. Li, Superbath Quantum Eigensolver (2024), arXiv:2412.19599 [quant-ph].

[55] F. Verstraete, M. Wolf, and J. Ignacio Cirac, Quantum computation and quantum-state engineering driven by dissipation, Nature Physics , 633 (2009).

[56] A. Micheli, B. Kraus, and H. Büchler, Quantum states and phases in driven open quantum systems with cold atoms, Nature Physics 4, 878 (2008).

[57] B. Horstmann, J. I. Cirac, and G. Giedke, Noise-driven dynamics and phase transitions in fermionic systems, Physical Review A 87, 012108 (2013).

[58] X. Mi et al., Stable quantum-correlated many-body states through engineered dissipation, Science 383, 1332 (2024).

[59] P. Stadler, M. Lodi, A. Khedri, R. Reiner, K. Bark, N. Vogt, M. Marthaler, and J. Leppäkangas, Demonstration of system-bath physics on a gate-based quantum computer, Phys. Rev. A 111, 022614 (2025).

[60] U. von Lüpke, I. C. Rodrigues, Y. Yang, M. Fadel, and Y. Chu, Engineering multimode interactions in circuit quantum acoustodynamics, Nature Physics 20, 564 (2024).

[61] A. B. Bozkurt, O. Golami, Y. Yu, H. Tian, and M. Mirhosseini, A mechanical quantum memory for microwave photons, Nature Physics , 1 (2025).

[62] J. Leppäkangas, P. Stadler, D. Golubev, R. Reiner, J.-M. Reiner, S. Zanker, N. Wurz, M. Renger, J. Verjauw, D. Gusenkova, S. Pogorzalek, F. Vigneau, P. Yang, W. Kindel, H.-S. Ku, F. Deppe, and M. Marthaler, Quantum algorithms for simulating systems coupled to bosonic modes using a hybrid resonator-qubit quantum computer (2025), arXiv:2503.11507 [quant-ph].

[63] T. Navickas, R. J. MacDonell, C. H. Valahu, V. C. Olaya-Agudelo, F. Scuccimarra, M. J. Millican, V. G. Matsos, H. L. Nourse, A. D. Rao, M. J. Biercuk, C. Hempel, I. Kassal, and T. R. Tan, Experimental Quantum Simulation of Chemical Dynamics, Journal of the American Chemical Society **147**, 23566 (2025).

[64] J. Whitlow, Z. Jia, Y. Wang, C. Fang, J. Kim, and K. R. Brown, Quantum simulation of conical intersections using trapped ions, Nature Chemistry **15**, 1509 (2023).

[65] V. So, M. Duraisamy Suganthi, A. Menon, M. Zhu, R. Zhuravel, H. Pu, P. G. Wolynes, J. N. Onuchic, and G. Pagano, Trapped-ion quantum simulation of electron transfer models with tunable dissipation, Science Advances **10** (2024).

[66] K. Sun, M. Kang, H. Nuomin, G. Schwartz, D. N. Beratan, K. R. Brown, and J. Kim, Quantum simulation of spin-boson models with structured bath, Nature Communications **16**, 4042 (2025).

[67] V. So, M. D. Suganthi, M. Zhu, A. Menon, G. Tomaras, R. Zhuravel, H. Pu, P. G. Wolynes, J. N. Onuchic, and G. Pagano, Quantum simulations of charge and exciton transfer in multi-mode models using engineered reservoirs (2025), arXiv:2505.22729 [quant-ph].

[68] J. Knörzer, T. Shi, E. Demler, and J. Cirac, Spin-Holstein Models in Trapped-Ion Systems, Phys. Rev. Lett. **128**, 120404 (2022).

[69] D. Motlagh, R. A. Lang, P. Jain, J. A. Campos-Gonzalez-Angulo, T. Zeng, A. Aspuru-Guzik, and J. M. Arrazola, Quantum Algorithm for Vibronic Dynamics: Case Study on Singlet Fission Solar Cell Design (2025), arXiv:2411.13669v2 [quant-ph].

[70] X. Dan, E. Geva, and V. S. Batista, Simulating Non-Markovian Quantum Dynamics on NISQ Computers Using the Hierarchical Equations of Motion, J. Chem. Theory Comput. **21**, 1530 (2025).

[71] W. Xue, Z. Zhang, S. K. So, Y. Song, Z. Wei, W. Ma, and H. Yan, Reducing the Excitonic Loss at Donor/Acceptor Heterojunction with Negligible Exciton Dissociation Driving Force, ACS Applied Energy Materials **5**, 9929 (2022).

[72] A. D. Somoza, N. Lorenzoni, J. Lim, S. F. Huelga, and M. B. Plenio, Driving force and nonequilibrium vibronic dynamics in charge separation of strongly bound electron–hole pairs, Commun Phys **6**, 1 (2023).

[73] A. A. Bakulin, A. Rao, V. G. Pavelyev, P. H. M. van Loosdrecht, M. S. Pshenichnikov, D. Niedzialek, J. Cornil, D. Beljonne, and R. H. Friend, The Role of Driving Energy and Delocalized States for Charge Separation in Organic Semiconductors, Science **335**, 1340 (2012).

[74] Simon Gélinas, Akshay Rao, Abhishek Kumar, Samuel L. Smith, Alex W. Chin, Jenny Clark, Tom S. van der Poll, Guillermo C. Bazan, and Richard H. Friend, Ultrafast Long-Range Charge Separation in Organic Semiconductor Photovoltaic Diodes, Science **343**, 512 (2014).

[75] Y. Song, S. N. Clafton, R. D. Pensack, T. W. Kee, and G. D. Scholes, Vibrational coherence probes the mechanism of ultrafast electron transfer in polymer–fullerene blends, Nature Communications **5**, 4933 (2014).

[76] A. D. Sio and C. Lienau, Vibronic coupling in organic semiconductors for photovoltaics, Physical Chemistry Chemical Physics **19**, 18813 (2017).

[77] Z. Xu, Y. Zhou, L. Groß, A. De Sio, C. Y. Yam, C. Lienau, T. Frauenheim, and G. Chen, Coherent Real-Space Charge Transport Across a Donor–Acceptor Interface Mediated by Vibronic Couplings, Nano Letters **19**, 8630 (2019).

[78] Z. Xu, Y. Zhou, C. Y. Yam, L. Groß, A. De Sio, T. Frauenheim, C. Lienau, and G. Chen, Revealing generation, migration, and dissociation of electron-hole pairs and current emergence in an organic photovoltaic cell, Science Advances **7** (2021).

[79] F. Mascherpa, A. Smirne, A. D. Somoza, P. Fernández-Acebal, S. Donadi, D. Tamascelli, S. F. Huelga, and M. B. Plenio, Optimized auxiliary oscillators for the simulation of general open quantum systems, Physical Review A **101**, 052108 (2020).

[80] D. Tamascelli, A. Smirne, S. Huelga, and M. Plenio, Nonperturbative Treatment of non-Markovian Dynamics of Open Quantum Systems, Physical Review Letters **120**, 030402 (2018).

[81] M. Cirio, N. Lambert, P. Liang, P.-C. Kuo, Y.-N. Chen, P. Menczel, K. Funo, and F. Nori, Pseudofermion method for the exact description of fermionic environments: From single-molecule electronics to the Kondo resonance, Phys. Rev. Res. **5**, 033011 (2023).

[82] M. Cirio, S. Luo, P. Liang, F. Nori, and N. Lambert, Modeling the unphysical pseudomode model with physical ensembles: Simulation, mitigation, and restructuring of non-Markovian quantum noise, Phys. Rev. Res. **6**, 033083 (2024).

[83] P. Menczel, K. Funo, M. Cirio, N. Lambert, and F. Nori, Non-hermitian pseudomodes for strongly coupled open quantum systems: Unravelings, correlations, and thermodynamics, Physical Review Research **6**, 033237 (2024).

[84] N. Lorenzoni, N. Cho, J. Lim, D. Tamascelli, S. F. Huelga, and M. B. Plenio, Systematic Coarse Graining of Environments for the Nonperturbative Simulation of Open Quantum Systems, Phys. Rev. Lett. **132**, 100403 (2024).

[85] A. D. Somoza, O. Marty, J. Lim, S. F. Huelga, and M. B. Plenio, Dissipation-Assisted Matrix Product Factorization, Physical Review Letters **123**, 100502 (2019).

[86] V. Kashyap, G. Styliaris, S. Mouradian, J. I. Cirac, and R. Trivedi, Accuracy Guarantees and Quantum Advantage in Analog Open Quantum Simulation with and without Noise, Physical Review X **15**, 021017 (2025), publisher: American Physical Society.

[87] B. Rost, L. Del Re, N. Earnest, A. F. Kemper, B. Jones, and J. K. Freericks, Long-time error-mitigating simulation of open quantum systems on near term quantum computers, npj Quantum Inf **11**, 1 (2025).

[88] V. May and O. Kühn, *Charge and Energy Transfer Dynamics in Molecular Systems*, 3rd ed. (WILEY-VCH Verlag GmbH & Co. KGaA, 2011).

[89] H.-P. Breuer and F. Petruccione, *The Theory of Open Quantum Systems* (Oxford University Press, 2007).

[90] P. D. Nation and M. Treinish, Suppressing quantum circuit errors due to system variability, PRX Quantum **4**, 010327 (2023).

[91] P. D. Nation, H. Kang, N. Sundaresan, and J. M. Gambetta, Scalable mitigation of measurement errors on quantum computers, PRX Quantum **2**, 040326 (2021).

[92] F. Dorfner, L. Vidmar, C. Brockt, E. Jeckelmann, and F. Heidrich-Meisner, Real-time decay of a highly excited charge carrier in the one-dimensional Holstein model, Phys. Rev. B **91**, 104302 (2015).

[93] N. J. Hestand and F. C. Spano, Expanded Theory of H- and J-Molecular Aggregates: The Effects of Vibronic Coupling and Intermolecular Charge Transfer, Chem. Rev. **118**, 7069 (2018).

[94] T. Jones, A. Brown, I. Bush, and S. C. Benjamin, Quest and high performance simulation of quantum computers, Scientific reports **9**, 10736 (2019).

[95] H. H. S. Chan, R. Meister, M. L. Goh, and B. Koczor, Algorithmic Shadow Spectroscopy, PRX Quantum **6**, 010352 (2025).

[96] J. D. Guimarães, J. Lim, M. I. Vasilevskiy, S. F. Huelga, and M. B. Plenio, Accelerating two-dimensional electronic spectroscopy simulations with a probe qubit protocol, Physical Review Research **7**, 023130 (2025).

[97] P. Klimov, J. Kelly, Z. Chen, M. Neeley, A. Megrant, B. Burkett, R. Barends, K. Arya, B. Chiaro, Y. Chen, A. Dunsworth, A. Fowler, B. Foxen, C. Gidney, M. Giustina, R. Graff, T. Huang, E. Jeffrey, E. Lucero, J. Mutus, O. Naaman, C. Neill, C. Quintana, P. Roushan, D. Sank, A. Vainsencher, J. Wenner, T. White, S. Boixo, R. Babbush, V. Smelyanskiy, H. Neven, and J. Martinis, Fluctuations of Energy-Relaxation Times in Superconducting Qubits, Physical Review Letters **121**, 090502 (2018).